

Loss of *Pip4k2c* confers liver-metastatic organotropism through insulin-dependent PI3K-AKT pathway activation

Received: 22 June 2023

Accepted: 8 December 2023

Published online: 29 January 2024

 Check for updates

Meri Rogava^{1,2,3}, Tyler J. Aprati^{4,24}, Wei-Yu Chi^{5,6,7,24}, Johannes C. Melms^{1,2,3}, Clemens Hug^{8,25}, Stephanie H. Davis⁸, Ethan M. Earlie^{5,6,7,9}, Charlie Chung¹⁰, Sachin K. Deshmukh¹¹, Sharon Wu¹¹, George Sledge¹¹, Stephen Tang^{1,2,3}, Patricia Ho^{1,2,3}, Amit Dipak Amin^{1,2,3}, Lindsay Caprio^{1,2,3}, Carino Gurjao^{1,2,3,12}, Somnath Tagore^{1,2,12}, Bryan Ngo⁶, Michael J. Lee¹³, Giorgia Zanetti³, Yiping Wang^{1,2,3,12}, Sean Chen^{1,2,3}, William Ge⁴, Luiza Martins Nascentes Melo¹⁴, Gabriele Allies¹⁴, Jonas Rösler¹⁴, Geoffrey T. Gibney¹⁵, Oliver J. Schmitz¹⁶, Megan Sykes³, Rémi J. Creusot³, Thomas Tüting¹⁷, Dirk Schadendorf¹⁴, Martin Röcken¹⁸, Thomas K. Eigentler¹⁹, Andrei Molotkov²⁰, Akiva Mintz²⁰, Samuel F. Bakhoun^{21,22}, Semir Beyaz¹⁰, Lewis C. Cantley²³, Peter K. Sorger⁸, Sven W. Meckelmann¹⁶, Alpaslan Tasdogan^{14,26}, David Liu^{4,26}, Ashley M. Laughney^{5,6,7,26} & Benjamin Izar^{1,2,3,12} ✉

Liver metastasis (LM) confers poor survival and therapy resistance across cancer types, but the mechanisms of liver-metastatic organotropism remain unknown. Here, through in vivo CRISPR–Cas9 screens, we found that *Pip4k2c* loss conferred LM but had no impact on lung metastasis or primary tumor growth. *Pip4k2c*-deficient cells were hypersensitized to insulin-mediated PI3K/AKT signaling and exploited the insulin-rich liver milieu for organ-specific metastasis. We observed concordant changes in *PIP4K2C* expression and distinct metabolic changes in 3,511 patient melanomas, including primary tumors, LMs and lung metastases. We found that systemic PI3K inhibition exacerbated LM burden in mice injected with *Pip4k2c*-deficient cancer cells through host-mediated increase in hepatic insulin levels; however, this circuit could be broken by concurrent administration of an SGLT2 inhibitor or feeding of a ketogenic diet. Thus, this work demonstrates a rare example of metastatic organotropism through co-optation of physiological metabolic cues and proposes therapeutic avenues to counteract these mechanisms.

Metastasis is a major determinant of mortality in patients with cancer¹, and metastatic patterns have important clinical and therapeutic implications². Liver metastasis (LM) occurs frequently across different cancer types, including melanoma and carcinomas of the colon, pancreas and breast³, and confers a poor prognosis and reduced response rates to

modern cancer therapies, such as immune checkpoint blockade, when compared to response rates in other common metastatic sites, such as the lung^{3–5}. The underlying mechanisms for these clinical phenotypes are poorly understood, partly because of difficulties in modeling of salient molecular underpinnings of metastatic organotropism preclinically.

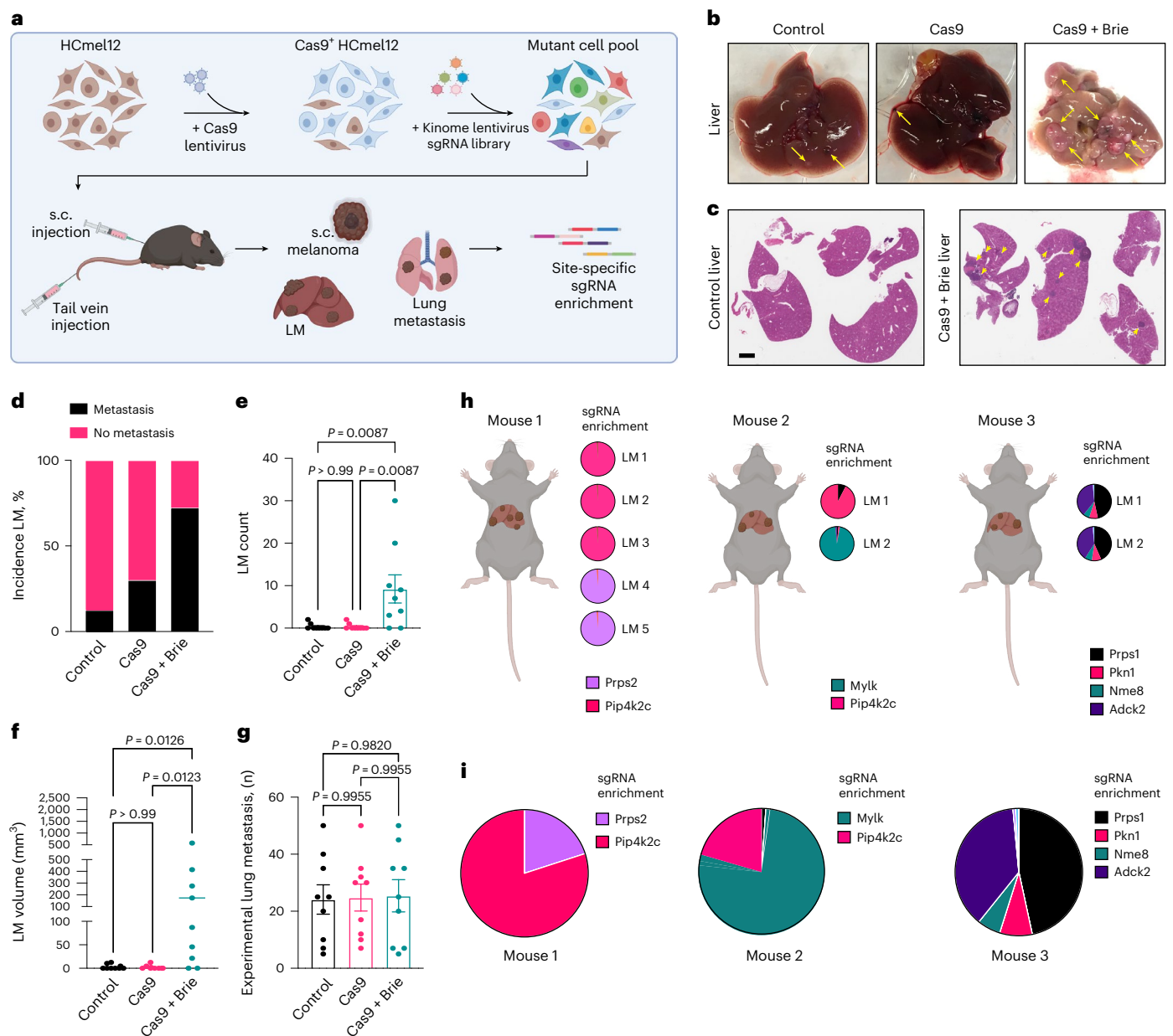


Fig. 1 | In vivo CRISPR–Cas9 screen identifies drivers of LM. a, Experimental design of in vivo CRISPR–Cas9 screen. **b**, Photographs of representative livers removed from animals in different groups as indicated. Yellow arrows indicate pigmented and nonpigmented liver metastases. **c**, Hematoxylin and eosin staining of representative sections of livers from indicated groups. Scale bar, 2 mm; $\times 40$ magnification; $n = 2$ independent experiments. **d**, Stack bar plots indicate fraction of animals bearing liver metastases across different experimental groups. **e**, LM count (e) and calculated LM disease burden (f) across experimental groups. **g**, Lung metastasis count in corresponding animals

from panel f. **h**, Exemplary distribution of sgRNA read fractions in three animals from the in vivo CRISPR–Cas9 metastasis screen. Pie charts show the fraction of the most abundant sgRNAs (sgRNAs with $>2\%$ of total reads) in each individual liver metastatic lesion next to each animal. **i**, Summary of fractions of enriched sgRNAs across all lesions from (h) within the individual mouse (larger pie charts below each animal). In panels **d–g**, $n = 9$ mice per group; bars represent mean \pm s.e.m.; one-way analysis of variance (ANOVA) Tukey’s multiple comparisons test. Data are representative of two independent experiments. Significance levels as indicated on top of each comparison.

Despite extensive efforts in a variety of disease contexts, divergent somatic mutations that fully explain organ-specific metastasis have not yet been identified^{6,7}. Although this may be due to the limited power of individual studies and extensive disease heterogeneity, it is likely that other biological factors underly cancer organotropism. Indeed, recent work in melanoma patients, for example, revealed a higher rate of chromosomal instability, a neural-like cell state and metabolic adaptation enriched in the brain metastases compared to extracranial metastases⁸. Whether similar organ-specific mechanisms exist for other sites is unknown.

The liver is the major metabolic organ, where a multitude of cues are generated, received and integrated, to regulate the supply of systemic nutrients, such as glucose and fatty acids⁹. Additionally, the liver has a dual blood supply via the hepatic artery and the portal vein, each of which may be a route for metastatic spread. There is also increasing evidence for hepatic modulation of local and peripheral immunity^{10,11}. These and other distinct organ features may contribute to the liver-metastatic niche in melanoma and other cancers.

To identify determinants of liver-metastatic organotropism in an unbiased fashion, we leveraged a syngeneic murine melanoma

model and performed large-scale CRISPR–Cas9 screens. We identified loss of *Pip4k2c* as driver of LM, but not extrahepatic metastasis. We showed that this organotropism is due to co-optation of the insulin-rich liver milieu, to which *Pip4k2*-deficient cells are hypersensitized, and unraveled downstream signaling and metabolic and transcriptomic adaptations enriched in liver metastases in mouse and patient tumors. We observed a paradoxical increase in LM burden in animals treated with systemic phosphoinositide 3-kinase (PI3K) inhibitors and showed that this was due to host-mediated responses that exacerbated the insulin-gradient, thereby promoting metastatic selectivity of *Pip4k2c*-deficient cells to the liver. A combination of PI3K inhibition with either systemic SGLT2 inhibition or feeding animals a ketogenic diet reduced LM burden while having little effect on other metastatic sites or primary tumor growth. Analyses and additional functional validation in prostate cancer and colorectal cancer models indicate a similar role of *Pip4k2c* in conferring LM, suggesting that the proposed biological and therapeutic principles may extend beyond melanoma.

Results

CRISPR screens reveal determinants of LM

To identify drivers of LM, we used a syngeneic melanoma model, HcMel12, which was derived from *Hgf/Cdk4^{R24C}* mice that spontaneously develop melanoma¹² and recapitulates the potential for LM and therapeutic response patterns seen in patients with metastatic melanoma^{13,14}. We performed a large-scale in vivo CRISPR–Cas9 screen in Cas9-expressing HcMel12 cells, perturbing 713 kinases in the mouse genome with 2,852 single-guide RNAs (sgRNAs) (four per target gene and 100 non-targeting control guides using the Brie library¹⁵) (Fig. 1a and Extended Data Fig. 1a–c). The edited cell pool (Cas9 + Brie), and Cas9-expressing cells without sgRNAs and parental cells, were injected via tail vein or subcutaneously implanted in C57BL/6 (B6) animals. In parallel, edited cell lines were maintained in vitro and collected at several time points for the duration of the experiment (Methods). Dissection of animals (Methods) revealed that the Cas9 + Brie group had a significantly higher rate of animals with LM (Fig. 1b–d), higher metastasis count per animal (Fig. 1e) and increased liver metastatic burden compared to the Cas9 and parental groups (Fig. 1f), whereas there was no difference in lung metastatic burden across these groups (Fig. 1g). This finding suggested that loss of kinases targeted by the Brie sgRNA library enhanced the liver metastatic potential of HcMel12 melanoma cells.

Before identifying perturbations that may alter liver metastatic potential, we first assessed the sgRNA library complexity within the plasmid pool, edited cells, transplanted primary tumors and distant metastasis (liver, lung and lymph nodes). Compared to the plasmid pool, cell line input and primary tumors, which showed preserved and co-correlated library diversity, sgRNA diversity decreased substantially in metastatic lesions (Extended Data Fig. 1d,e) across different sites, whereas samples from the same metastatic sites showed stronger co-correlation (Extended Data Fig. 1d). In line with this, principal-component analysis (PCA) of sgRNA representations revealed clades of metastases and transplanted tumors/cell lines along PC1 (explaining 49.7% of variability) and PC2 (5.4% of variability) (Extended Data Fig. 1f). Next, we identified sgRNAs targeting essential genes (for example, *Plk1*, *Cdk7* and *Cdk12*) that were depleted after 14 days of editing in cells prior to injection into animals (Extended Data Fig. 2a–c and Supplementary Table 1). Additionally, sgRNAs targeting *Cdk4*, a known dependency in HcMel12, were also significantly depleted (\log_2 fold change = -10.206 , false discovery rate (FDR) < 0.06). Compared to edited cells before injection, primary tumors showed significant depletion of multiple genes, including *Jak1* and *Jak2*, suggesting that the Jak/Stat pathway may be important for tumor growth, as absence of intact *Jak1/Jak2* has been implicated in immune evasion¹⁶. *Stk11* was also depleted in primary tumors; loss of *Stk11* (encoding for Lkb1) promotes

metastasis and confers therapy resistance¹⁷. The most strongly enriched perturbation involved in primary tumor growth was loss of *Dapk3* (\log_2 fold change = 4.3693, FDR < 0.007) (Extended Data Fig. 2b and Supplementary Table 2), a putative tumor suppressor gene whose deleterious mutations or loss occurs in up to ~7% of melanomas¹⁸. Together, these data suggested that the conducted screen was robust and yielded data known and unknown biology, with sgRNA diversity reducing along the metastatic progression axis. This observation suggested that a small fraction of perturbations may determine metastatic potential¹⁹.

We next sought to identify sgRNAs associated with metastatic potential to the liver. We used three criteria to nominate such putative drivers: sgRNAs that (1) are enriched with an FDR < 0.1 and/or (2) account for >2% of sequencing reads within a given lesion and/or (3) are enriched in two or more biological replicates. We identified 80 sgRNAs that meet one (65), two (17) or all (2) of these criteria (Supplementary Table 3). Among the genes targeted by these sgRNAs are those involved in cell motility (*Tesk1*, *Pkn1* and *Mylk4*)^{20–22}, nucleotide homeostasis and metabolism (*Prps1*, *Prps2*, *Adck2* and *Nme8*)²³ or modulation of insulin sensing (*Trib1* and *Pip4k2c*)^{24–26} or function as tumor suppressors (*Fgfr3*)²⁷, such that the loss of these genes would promote hallmarks of metastasis. The top hit in this screen by all applied metrics was loss of *Pip4k2c*, which encodes phosphatidylinositol-5-phosphate 4-kinase type 2 gamma. Specifically, loss of *Pip4k2c* was the most enriched perturbation in 5 of 14 (~36%) investigated liver metastatic lesions. In all of these lesions, sgRNAs targeting *Pip4k2c* accounted for the majority of sequencing reads, whereas in four of these five lesions, this perturbation accounted for >98% of sequencing reads (Fig. 1h,i and Extended Data Fig. 2d). Furthermore, loss of *Pip4k2c* was the only perturbation (at an FDR < 0.06) that was highly specific to LM (Extended Data Fig. 2e). These findings suggest that *Pip4k2c* loss may uniquely promote LM.

Pip4k2c loss sensitizes cells to insulin-mediated signaling

Pip4k2c is part of the Pip4k family that consists of three isoforms in both mice and humans²⁴. The role of these kinases is poorly understood, but recent work suggests that Pip4k, and the gene product of *Pip4k2c*, suppress Pip5k activity in response to insulin. This results in reduced production of phosphatidylinositol-4-5-bisphosphate (PI(4,5)P₂), the substrate of PI3K, which converts PI(4,5)P₂ to phosphatidylinositol-3-4-5-triphosphate (PI(3,4,5)P₃) to subsequently activate AKT. Thus, we hypothesized that loss of *Pip4k2c* would lead to hyperactivation of the PI3K/AKT pathway in response to insulin. We hypothesized that because the liver is the organ with the highest insulin concentration (outside of the pancreas, where it is produced), *Pip4k2c*-loss mediated PI3K/AKT hypersensitization to insulin in tumor cells could encourage formation of an organ-specific metastatic niche.

To test whether *Pip4k2c* promotes PI3K/AKT hypersensitivity to insulin in melanoma cells, we generated HcMel12-*Pip4k2c*-KO cell lines (*Pip4k2c*^{KO}) using four different sgRNAs, including the top enriched sgRNA in our in vivo screen (Extended Data Fig. 3a,b). We next determined the impact of *Pip4k2c*^{KO} on downstream PI3K/AKT pathway activation in response to insulin. Compared to parental cells, insulin stimulation of *Pip4k2c*^{KO} resulted in higher and prolonged induction of phosphorylated AKT in both murine HcMel12 and the human melanoma model A375 (Fig. 2a,b and Extended Data Fig. 3c–e) and increased phosphorylation of insulin receptor (INSR) (Extended Data Fig. 3f) and showed increased cell migration capacity, whereas the proliferation rate was not altered (Extended Data Fig. 3g–j). Bulk RNA sequencing (RNA-seq) of parental compared to *Pip4k2c*^{KO} cells stimulated with insulin revealed enrichment of mTOR pathway activity (Extended Data Fig. 3k and Supplementary Table 4). We rescued *Pip4k2c*^{KO} with one of two open reading frames (ORFs): full-length (*Pip4k2c*^{Rec}) or allosteric-domain-deficient (aa69-75 (VMLPDD → EIFLNN)) (*Pip4k2c*^{AD}), which was previously implicated in Pip4k2c function²⁴ (Extended Data Fig. 3l–n). Although *Pip4k2c*^{AD} continued to demonstrate high baseline and insulin-mediated Akt phosphorylation, *Pip4k2c*^{Rec} had lower p-Akt

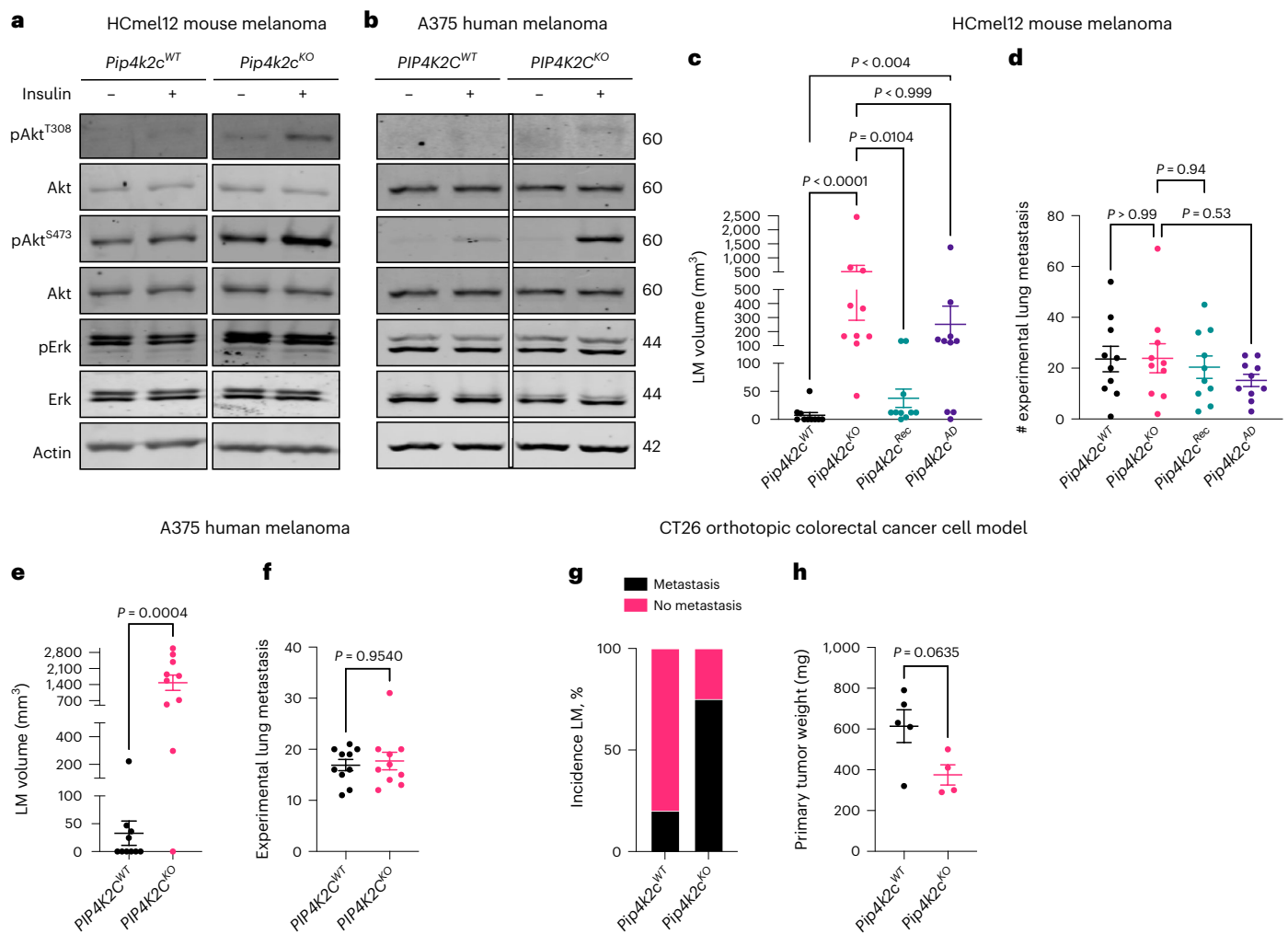


Fig. 2 | Loss of *Pip4k2c* enhances sensitivity to insulin and promotes LM, but not lung metastasis. a, b, Immunoblots showing phosphorylated and total protein of key signaling nodes of p-Akt^{S473} and p-Akt^{T308} in wild-type (WT) or *Pip4k2c*^{KO} cells in (a) HCmel12 and (b) A375 melanoma cell models with (+) or without (-) insulin (250 ng ml⁻¹) stimulation. **c, d**, LM disease burden (mm³) and lung metastases count following tail vein injection of parental and *Pip4k2c* KO HCmel12 melanoma in C57BL/6 mice. **e, f**, Liver and lung metastasis burden following tail vein injection of parental and *PIP4K2C* KO A375 melanoma cells

in NSG mice. **g**, Incidence of macroscopic LM in animals following orthotopic injection of parental or *Pip4k2c* KO CT26 colorectal cancer cells in BALB/c mice. **h**, Comparison of tumor weight of primary tumors from experiment shown in panel g. In panels c–f, $n = 10$ mice per group; in panels g and h, $n = 4–5$ mice per group; mean \pm s.e.m., one-Way ANOVA Tukey's multiple comparisons test (c, d) and Mann–Whitney two-tailed test (e–g). Data are representative of three (c, d), two (e, f) or one (h, g) independent experiments. Significance levels are indicated on top of each comparison.

levels in both human and murine melanoma models (Extended Data Fig. 3l–n). This finding suggests that lack of the allosteric domain, but not the kinase domain of *Pip4k2c*, is sufficient to confer hypersensitization to insulin and is consistent with prior work showing that *Pip4k2c* has very poor kinase activity²⁴. Treatment with the pan-PI3K inhibitor GDC-0941 (pictilisib) (with and without insulin stimulation) (Extended Data Fig. 3l–n) completely abrogated baseline Akt phosphorylation in cells with all of these genotypes, whereas insulin partly rescued PI3K activity (Extended Data Fig. 3l–n), which is consistent with a prior report²⁸. We also tested the PI3K alpha inhibitor BYL-719, which overall showed lower efficacy but similar results for insulin-mediated bypass activation (Extended Data Fig. 3l–n).

Loss of *Pip4k2c* confers liver-metastatic organotropism

To validate the role of *Pip4k2c* loss in vivo, we next injected either parental (*Pip4k2c*^{WT}), *Pip4k2c*^{KO}, *Pip4k2c*^{Rec} or *Pip4k2c*^{AD} HCmel12 melanoma cells via tail vein in B6 mice. *Pip4k2c*^{KO} resulted in a significantly increased LM burden that was rescued by *Pip4k2c*^{Rec}, but not *Pip4k2c*^{AD} (Fig. 2c). Importantly, none of these perturbations altered lung metastatic burden

(Fig. 2d). Consistently, loss of *PIP4K2C* in human melanoma cell line A375 conferred significantly increased metastasis to the liver, but not to the lung (Fig. 2e, f and Extended Data Fig. 3o). To determine whether *Pip4k2c* loss plays a role in LM development in other cancers that also frequently metastasize to the liver, we generated *Pip4k2c* KO in a colorectal cancer cell line (CT26) and orthotopically implanted these or parental cells into the colonic submucosa of BALB/c mice. Primary tumors arising from parental CT26 resulted in LM in 20% of animals, whereas *Pip4k2c*^{KO} cells gave rise to LM in 75% of animals (Fig. 2g). Notably, *Pip4k2c*^{KO} gave rise to smaller primary colorectal tumors (Fig. 2h), thus indicating that higher rates of LM development were due to increased invasive capacity, as observed in melanoma models (Fig. 2c, e). Together, these results suggest that loss of *Pip4k2c* hypersensitizes cancer cells to insulin-mediated PI3K/AKT hyperactivation and thereby mediates metastasis specifically to the liver, but not to the lung.

Systemic PI3K inhibition enhances LM through host effects

Because PI3K inhibition could abrogate PI3K/AKT signaling in vitro (Extended Data Fig. 3m, n), we reasoned that systemic treatment with

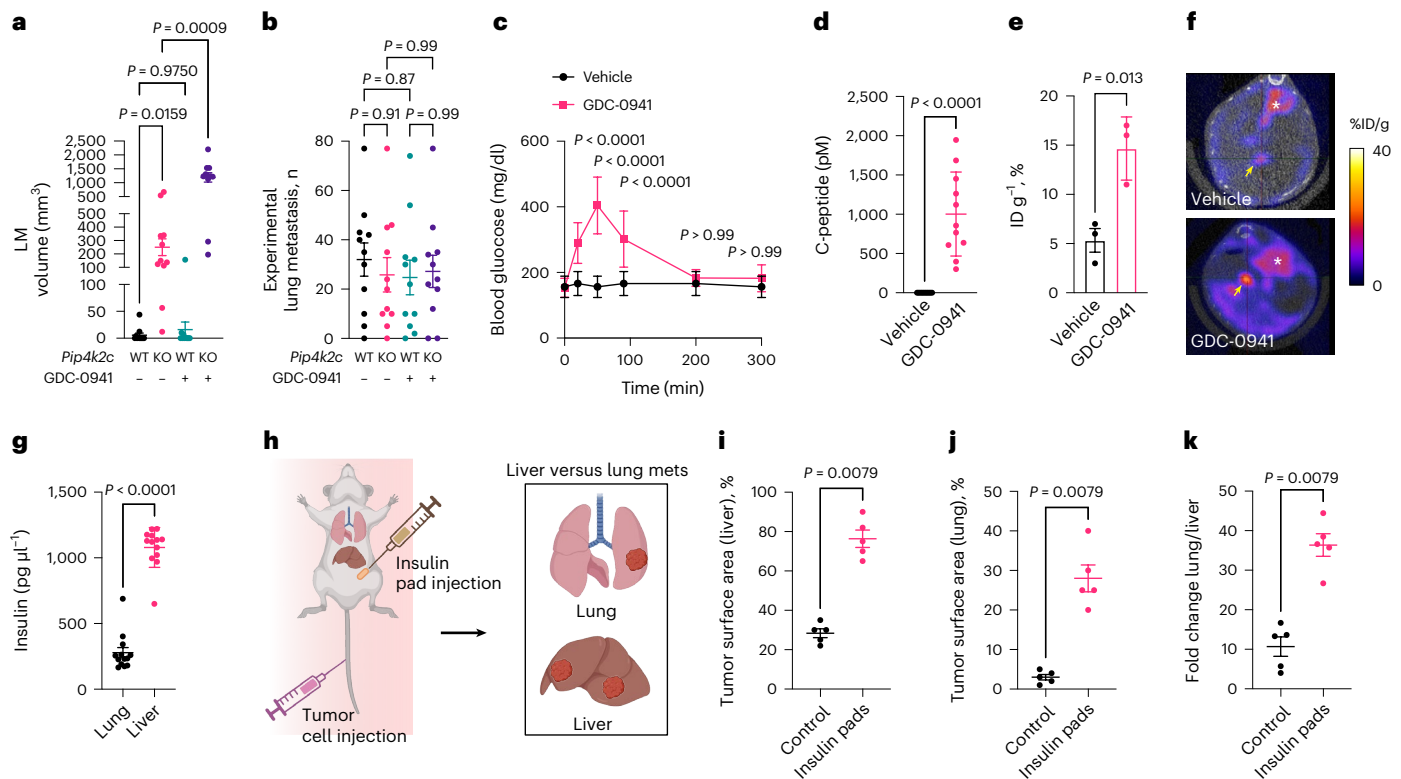


Fig. 3 | Systemic feedback loop induced by PI3K inhibitor treatment *in vivo* promotes liver organotropism in *Pip4k2c*-deficient tumors in an insulin-dependent manner. **a**, Liver metastasis disease burden (mm^3) upon tail vein injection of parental and *Pip4k2c* KO HcMel12 melanoma cells with and without GDC-0941 treatment (daily, 5 days a week, 100 mg kg^{-1}). **b**, Lung metastasis burden (metastasis count) in corresponding animals from panel **a** ($n = 10$ mice per group; mean \pm s.e.m.). **c**, Blood glucose levels (mg dl^{-1}) in mice following treatment with GDC-0941 or vehicle control over time (minutes). **d**, C-peptide levels (in pM) in corresponding animals from panel **c**; $n = 10$ mice per group; mean \pm s.e.m.; two-way ANOVA Tukey's multiple comparisons test (**a,b**) and Mann-Whitney two-tailed test (**c,d**). Significance levels as indicated. **e,f**, Quantification of FDG- μ PET (18F-fluorodeoxyglucose in percent of injected dose (ID) per gram (**e**)) and

corresponding LM uptake (**f**) 60 min after GDC-0941 administration or vehicle control. Yellow arrows indicate individual liver metastatic lesions. Cardiac FDG uptake is visualized (asterisk); $n = 3$ mice per group, mean \pm s.e.m.; unpaired two-sided-t-test (**e**). **g**, Insulin levels ($\text{pg } \mu\text{l}^{-1}$) in liver and lung tissues from non-tumor-bearing mice. $n = 10$ mice per group, mean \pm s.e.m.; Mann-Whitney two-tailed test. **h**, Schematic illustrating the insulin pad experiment in mice. mets, metastases. **i,j**, Percentage of metastasis surface area in liver (**i**) and lung (**j**) of animals implanted with a control pad or insulin pad, followed by injection of tumor cells via tail vein in NSG mice. **k**, Ratio of lung over liver metastatic burden from experiment (**i,j**); $n = 5$ mice per group; mean \pm s.e.m.; Mann-Whitney two-tailed test; Data are representative of three (**a-d**) or two (**e-k**) independent experiments. Significance levels are indicated on top of each comparison.

the same drug would reduce LM burden *in vivo*. We injected parental or *Pip4k2c*^{KO} cells and treated animals with either vehicle control or GDC-0941 (Methods). Surprisingly, we found that liver-metastatic burden was significantly increased in animals bearing *Pip4k2c*^{KO} tumor cells, whereas lung metastatic burden was not altered (Fig. 3a,b). We reasoned that this paradoxical increase in LM burden in *Pip4k2c*^{KO} tumor-bearing mice in response to PI3K inhibition may be explained by the effects of the drug on the host, which may promote LM in an insulin-dependent manner. Indeed, treatment with GDC-0941 resulted in a significant increase in blood glucose levels that peaked 60 min after administration and was sustained for at least 90 min (Fig. 3c). Accordingly, the levels of C-peptide, a short amino-acid polypeptide of pro-insulin and equimolar surrogate for insulin production, were significantly increased in GDC-0941-treated animals with either *Pip4k2c*^{WT}- or *Pip4k2c*^{KO}-bearing tumors (Fig. 3d and Extended Data Fig. 3p), suggesting that these differences in metastatic burden are explained by host responses to this treatment. To assess whether GDC-0941 induced glucose and insulin spikes influenced metastatic tumor cell sensitivity to insulin *in situ*, we treated *Pip4k2c*^{KO} LM-bearing mice with GDC-0941 or vehicle control. After 60 min, when blood glucose concentration peaks following PI3K inhibitor treatment, we performed [F18] fluorodeoxyglucose (FDG) micro-positron emission tomography (μ PET). We found that *Pip4k2c*^{KO} LM had a threefold increase in FDG uptake in PI3K-inhibitor-treated

mice (Fig. 3e,f). Lastly, we directly measured homeostatic levels of insulin in livers and lungs, confirming significantly higher levels in the hepatic environment (Fig. 3g). If high insulin concentration in the liver is an important cue for liver-metastatic organotropism, we reasoned that increasing insulin levels in the lung should increase the rate of metastasis to this organ. To test this hypothesis, we subcutaneously implanted mice with slow-release insulin pads (Fig. 3h), which continuously deliver high systemic levels of insulin, followed by injection of cancer cells via tail vein, and we determined liver and lung metastatic burden. Although insulin delivery resulted increased metastatic burden was increased in both liver and lung (Fig. 3i), there was a significantly elevated lung-metastatic potential compared to control pad-implanted animals (Fig. 3j,k), suggesting that some disease burden was diverted to the lungs with higher local insulin levels. Together, these results suggest that *Pip4k2c*^{KO} cells efficiently co-opt the insulin-rich liver milieu for metastasis, and this can be further enhanced by host responses to PI3K inhibition.

Human and murine LMs exhibit distinct metabolic adaptations

To further examine cancer cell states in liver compared to lung metastases, we performed single-cell RNA-sequencing (scRNA-seq) of eight mice with concurrent liver and lung metastases. Following rigorous

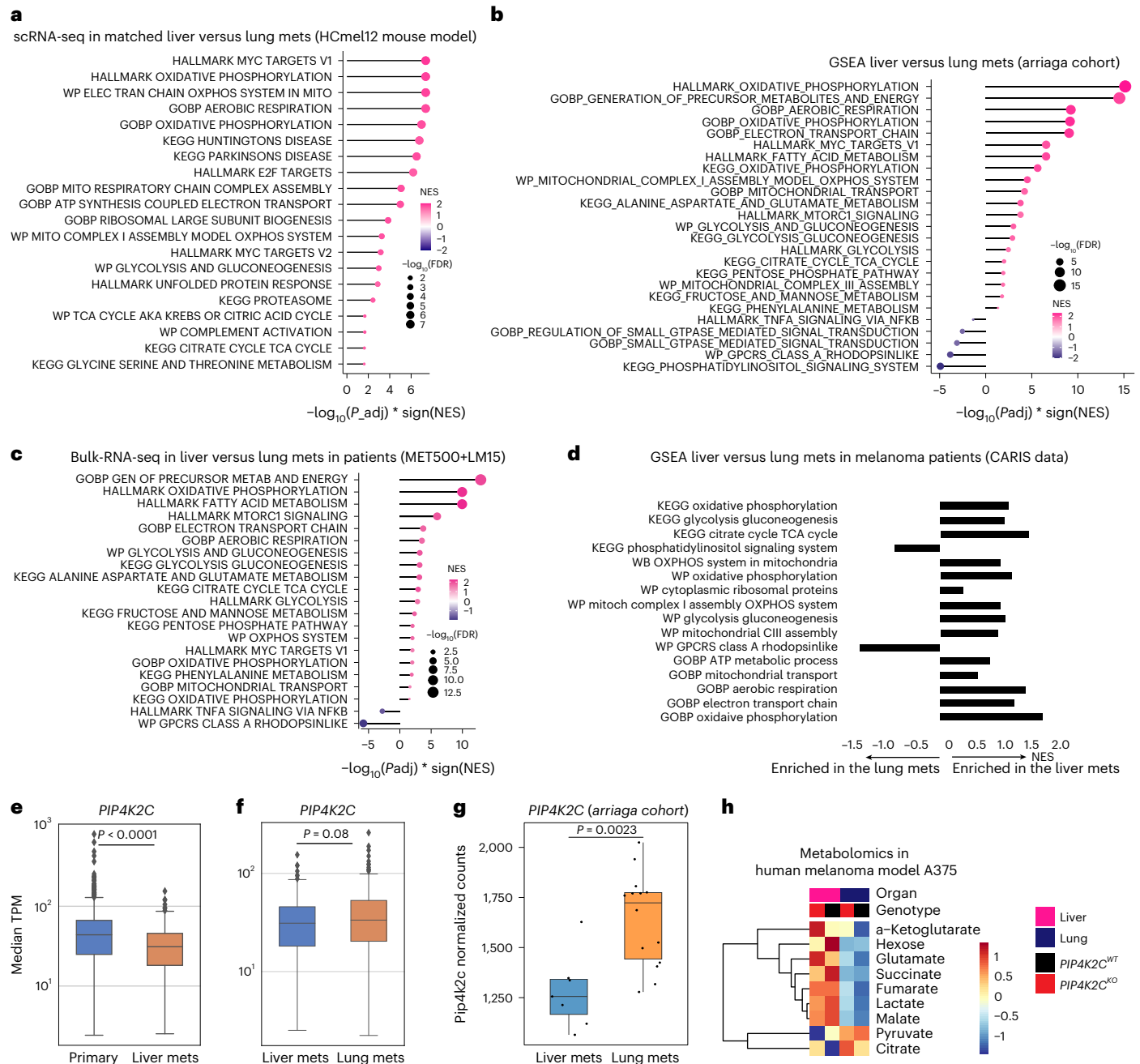


Fig. 4 | Multiomics analysis of human and mouse liver and lung metastasis.

a, Top enriched pathways (adjusted P (P_{adj}) < 0.05 , top five pathways per gene set ranked by normalized enrichment score) of cancer cells isolated from concurrent liver ($n = 8$ specimens, pink) versus lung ($n = 8$ specimens, purple) metastases in mice injected with HCmel12 melanoma cells. **b**, Pathway enrichment (FDR q -value < 0.05) within Arriaga et al. cohort comparing liver ($n = 7$ specimens, pink) versus lung ($n = 14$ specimens, purple) metastases in a prostate cancer metastasis model. **c**, Enriched pathways (FDR q -value < 0.05) in liver ($n = 78$ patients, Met500; $n = 15$ patients, LM15, pink) vs lung ($n = 16$ patients, Met500, purple) metastases across tumors. **d**, Enriched pathways (adjusted P value < 0.05) in liver ($n = 364$) versus lung ($n = 743$) metastases in patients with melanoma tumors; FDR value for GSEA was obtained by Benjamin–Hochberg correction. **e, f**, Expression of *PIP4K2C* in melanoma patient tumors comparing primary cutaneous tumors ($n = 2,404$ patients) versus liver ($n = 364$) (e), and

liver ($n = 364$ patients) versus lung ($n = 743$ patients). Mann–Whitney two-tailed test. **g**, Expression of *Pip4k2c* from the Arriaga et al. cohort comparing liver ($n = 7$ specimens) versus lung ($n = 14$ specimens), Wilcoxon rank-sum test. For all box plots, n refers to the number of samples, and P refers to the P value. The center line indicates the median, the box limits denote the first and third quartiles and the whiskers indicate the lowest or highest data points at the first quartile minus or plus 1.5 times the interquartile range; Significance levels as indicated. **h**, Cumulative results of selected top differentially abundant metabolites in animals with liver and/or lung metastases following injection with either parental (*PIP4K2C*^{WT}) or *PIP4K2C*^{KO} A375 human melanoma cells; $n = 5$ mice per group; unpaired two-sided t -test. Lactate ($P = 2.36727 \times 10^{-5}$), pyruvate ($P = 0.03$), citrate ($P = 0.25$), a-ketoglutarate ($P = 0.18$), succinate ($P = 0.004$), fumarate ($P = 0.04$), malate ($P = 0.04$) and hexose ($P = 6.72275 \times 10^{-6}$).

quality control (Methods and Supplementary Tables 4 and 5), a total of 95,606 cell transcriptomes were included for downstream analyses. We identified tumor cells by their expression of melanocytic lineage

markers, including *Mitf*, *Mlana*, *Dct*, *Tyr* and *Tyrp1*. Differential gene expression and subsequent gene set enrichment analysis (GSEA) of melanoma cells revealed strong enrichment of metabolic pathways in

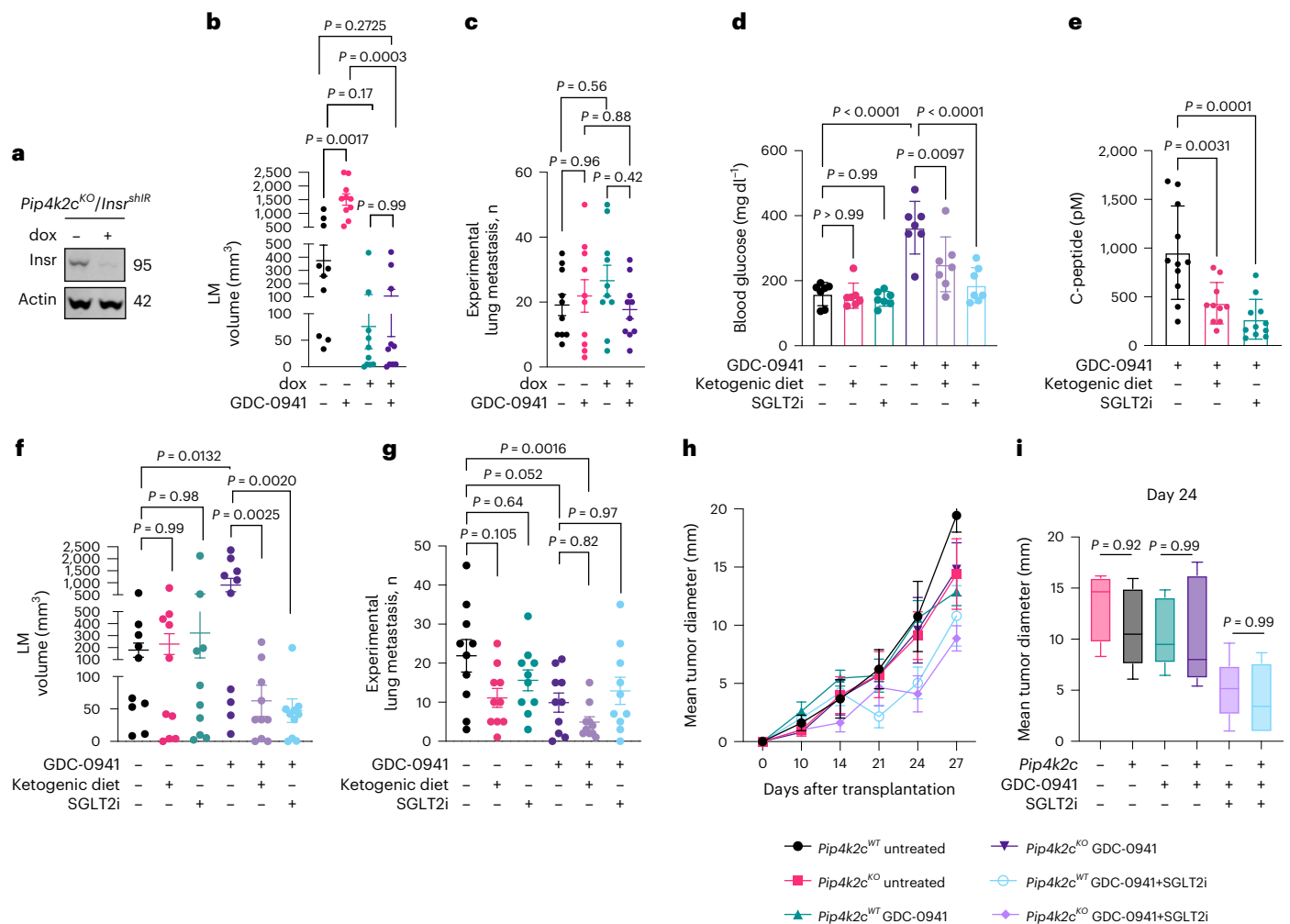


Fig. 5 | Genetic, dietary or pharmacological strategies disrupting systemic host effects of PI3K inhibition reduces metastatic liver organotropism.

a, Immunoblot probing Insr in *Pip4k2c^{KO}/Insr^{shIR}* cells before use for in vivo experiments (in panels b and c). **b**, Liver metastasis disease burden (in mm³) following tail vein injection of *Pip4k2c^{KO}/Insr^{shIR}* without dox, GDC-0941 alone, dox-induced *Insr* knockdown alone and a combination of dox-induced *Insr* knockdown and GDC-0941. **c**, Lung metastasis burden (metastasis count) in corresponding animals from panel b; *n* = 10 mice per group. **d**, Blood glucose levels (mg dl⁻¹) measured in mice (*n* = 7 mice per group) following treatment with indicated diet or drugs (30 min after administration) or vehicle control. **e**, C-peptide levels (pM) following treatment with indicated combinations of GDC-0941 with SGLT2 inhibition or animals fed with ketogenic diet (*n* = 11 mice

per group). **f**, Liver metastasis disease burden (mm³) following tail vein injection of *Pip4k2c^{KO}* cells with drug treatments (SGLT2i, GDC-0941), ketogenic diet or combinations thereof in indicated groups. **g**, Lung metastasis burden (metastasis count) in corresponding animals from panel f; *n* = 10 mice per group, mean ± s.e.m.; **h**, Tumor growth of subcutaneously injected HcMel12 parental or *Pip4k2c^{KO}* melanoma cell lines following no treatment, treatment with GDC-0941 alone or with the combination of GDC-0941 plus SGLT2 inhibition; *n* = 5 mice per group, mean ± s.e.m. **i**, Tumor diameter at day 24 in indicated treatment and genotype groups from panel h. Box plots denote the minima, maxima and median in panel h. Statistical significance was determined using one-way ANOVA Tukey's multiple comparisons test (b–h). Data are representative of three (b–g) or two (h, i) independent experiments. Significance levels are indicated.

cells isolated from liver metastases, including regulation of oxidative phosphorylation (Fig. 4a and Extended Data Fig. 4a–g). In support of the observations in melanoma, we analyzed another bulk RNA-seq data set of a prostate cancer model²⁹ that develops metastasis to multiple organs, including to liver, lung and bone, and found the same metabolic pathway enrichment in liver compared to lung metastases (Fig. 4b).

To determine the relevance of these phenotypic differences in a patient context, we performed RNA-seq of melanoma LMs and combined these with publicly available data (Methods)³⁰, totaling 252 metastasis transcriptomes, including 93 liver metastases (Supplementary Tables 4 and 5). Comparison of LM transcriptomes with lung metastases revealed strong enrichment of metabolic pathways in LM, including tricarboxylic acid (TCA) cycle, oxidative phosphorylation and mTORC1 signaling (Fig. 4c, Extended Data Fig. 4h–j and Supplementary Tables 4 and 5). These results were maintained when including only samples with high purity, reducing potential transcriptome

contamination by healthy hepatocytes (Extended Data Fig. 4j, k and Supplementary Tables 4 and 5). Additionally, our scRNA-seq pathway analyses were exclusively performed on tumor cells yielded comparable results. To comprehensively determine the role of these observations in a large real-world data set, we analyzed 3,511 cutaneous melanoma patients, including 2,404 primary cutaneous melanomas (PCMs), 364 LMs and 743 lung metastases (Supplementary Table 4). For all specimens, tumor regions were enriched through macro-dissecting and profiled using RNA-seq and exome sequencing (either whole-exome or 592 gene panel DNA-sequencing) at Caris Life Sciences. We found strong enrichment of metabolic pathways, including TCA cycle and oxidative phosphorylation in LMs compared to PCMs and lung metastases (Fig. 4d), which mirrored our observations in mouse models (Fig. 4a, b) and publicly available patient data analyzed here (Fig. 4c). Overall, these transcriptomics data suggest that cancer cells in the liver enrich for key metabolic pathways when compared to other metastatic sites,

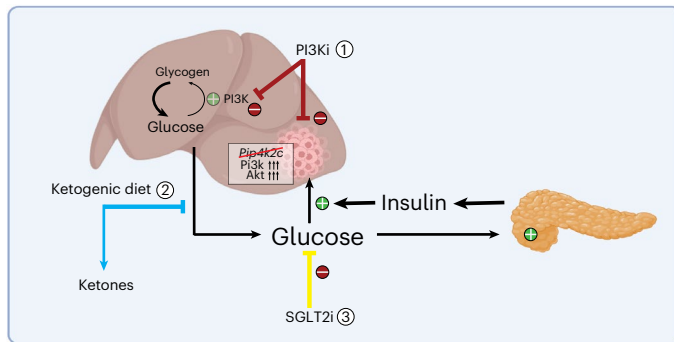


Fig. 6 | Schematic of liver metastatic organotropism. Model illustrating increased liver metastatic burden in animals injected with *Pip4k2c^{KO}* cells. (1) Effects of systemic PI3K inhibition (PI3Ki). Strategies to overcome compensatory feedback loop and increased liver metastatic burden with either (2) ketogenic diet or (3) SGLT2 inhibition (SGLT2i).

both in melanoma and other cancers. In the same patient cohort, we found that *PIP4K2C*, but not *PIP4K2A* or *PIP4K2B*, had a lower expression in LMs compared to PCMs and lung metastases ($P < 0.0001$ and $P = 0.08$, respectively) (Fig. 4c,f and Extended Data Fig. 4l,m). Additionally, comparison of genomics of LMs with either PCM or lung metastases in these patients showed distinct distribution of common oncogenic driver mutations, including *BRAF*, *NRAS* and *NF1*, and revealed an enrichment of the less commonly mutated (in melanoma) gene *PIK3CA* encoding for p110 α , the catalytic subunit of PI3K in LMs compared to PCMs and lung metastases (4.27% versus 1.21%, $P = 0.003$, and 4.27% versus 2.34%, $P = 0.19$, respectively) (Extended Data Fig. 4n). Similarly, we found lower expression of *Pip4k2c*, but not *Pip4k2a/b*, in LMs compared to other metastatic sites in the Arriaga et al. prostate cancer metastatic mouse model data (Fig. 4g and Extended Data Fig. 4o).

We next sought to directly measure potential differences in metabolites between liver and lung metastases. For this purpose, we injected A375 cells (parental or *Pip4k2c^{KO}*) and collected liver and lung metastases (Methods). We performed mass spectrometry on five liver and five concurrent lung metastases from animals injected with *Pip4k2c^{KO}* cells and three liver and five lung metastases from mice injected with *Pip4k2c^{WT}* cells. PCA demonstrated that across and within each genotype, disease site (liver versus lung) was the most important driver of variability in metabolic profiles (Extended Data Fig. 5a,b and Supplementary Table 6). Several key metabolites of the TCA cycle, including α -ketoglutarate, succinate, fumarate and malate, were found at higher abundances in liver compared to lung metastases (Fig. 4h and Extended Data Fig. 5c–e), consistent with the findings indicated from our transcriptomics analyses (Fig. 4a–d).

INSR is necessary for liver-metastatic organotropism

Our data suggest that co-optation and metabolic adaptations to the insulin-rich liver milieu are strongly associated with liver-metastatic organotropism. To determine whether insulin acting on cancer cells is necessary for both liver-metastatic organotropism and increased disease burden in response to systemic PI3K inhibition, we transduced parental or *Pip4k2c^{KO}* cells with a doxycycline (dox)-inducible short hairpin RNA (shRNA) targeting the insulin receptor (*Insr*) to generate otherwise isogenic, conditional *Insr* knockdown (*Insr^{shIR}*) or *Pip4k2c^{KO}/Insr^{shIR}* cells (Fig. 5a). As expected, we found an impaired induction of Akt phosphorylation in response to insulin in both dox-induced *Insr^{KO}* and *Pip4k2c^{KO}/Insr^{shIR}* cells, compared to their non-dox-treated counterparts. Across all conditions, GDC-0941 effectively abrogated p-AKT (Extended Data Fig. 6a). Next, we injected mice with dox-treated or untreated *Pip4k2c^{KO}/Insr^{shIR}* tumor cells followed by treatment with vehicle or GDC-0941. *Insr* knockdown alone resulted in LM reduction compared to non-dox-treated animals (albeit not statistically significant),

and in mice treated with GDC-0941, *Insr* knockdown in *Pip4k2c^{KO}* tumor cells resulted in a significantly reduced LM burden (Fig. 5b). Across all conditions, there was no change in lung metastasis burden (Fig. 5c). Overall, these results suggest that although GDC-0941 effectively abrogates Akt phosphorylation in vitro, host responses to the drug and subsequent insulin-dependent circuitry increase metastasis to the liver, but not the lung.

Combination interventions reduce LM burden

We reasoned that abolishing the PI3K-inhibitor-induced forward loop could reduce liver metastatic burden. To test this, we treated animals with an inhibitor of sodium glucose co-transporter 2 (SGLT2i) that inhibits glucose reuptake in the kidney, thereby preventing spikes in insulin levels, or we fed animals a ketogenic diet that depletes glycogen storage (Methods). Peak blood glucose and plasma C-peptide levels were strongly reduced when combining GDC-0941 with SGLT2i or a ketogenic diet (Fig. 5d,e). In *Pip4k2c^{KO}* LM-bearing animals, combination of either SGLT2i or a ketogenic diet with GDC-0941 significantly reduced LM compared to animals receiving GDC-0941 alone (Fig. 5f). Notably, a combination of ketogenic diet with GDC-0941 also significantly reduced lung metastatic burden, whereas SGLT2i plus GDC-0941 selectively targeted liver-metastatic disease (Fig. 5g), suggesting that addition of SGLT2i and a ketogenic diet to PI3K inhibitor could circumvent GDC-0941-induced increase in LM. Importantly, compared to parental cells, loss of *Pip4k2c* had no differential impact on growth of subcutaneously implanted tumors or responses to GDC-0941 or GDC-0941 plus SGLT2i (Fig. 5h,i and Extended Data Fig. 6b). This finding is consistent with the initial CRISPR–Cas9 screen and suggests PI3K-inhibitor-based therapeutic combinations are critical for abrogating insulin-mediated circuits that are most pronounced in LM (Fig. 6).

Discussion

Not all metastatic sites are created equal. Compared to other sites, metastasis to the liver confers a poorer prognosis across multiple cancer types and reduced responses to modern cancer therapies^{4,31,32}. Mechanisms that determine a cancer cell's metastatic fate toward one organ site over another are poorly understood and are not sufficiently accounted for by a model of serial, divergent acquisition of somatic mutations^{33,34}. The fact that cancer types with different oncogenic dependencies and distinct lineages exhibit a shared preponderance for metastasis to a specific organ (for example, LM in both melanoma and colorectal cancer) suggests that target-organ-specific adaptations occur and may be determined by the required metabolic requirements and phenotypic plasticity³⁵.

Dissecting the molecular underpinnings of LM has been challenging due to limited preclinical models that recapitulate the liver-metastatic cascade in the presence of an intact immune system. Recent studies using intrahepatic or portal/splenic vein injections of cancer cells revealed important but narrow aspects of LM biology and growth^{36,37}. Here, we leveraged a syngeneic melanoma model that has the potential to develop LM upon tail vein injection that recapitulates several bottlenecks in the LM cascade. We performed functional screens and find that cancer cell-intrinsic loss of *Pip4k2c* promotes melanoma cell metastasis by co-opting an insulin-rich liver milieu via activation of the PI3K/AKT pathway (Fig. 6) without altering primary tumor growth or their metastatic potential to other organ sites (for example, lung). Importantly, this mechanism may apply for both routes of dual blood supply to the liver, as we demonstrate increased LM via systemic circulation in our melanoma model and a prostate cancer model, and via portal vein, using a colorectal cancer model implanted into the colonic submucosa.

Recent studies demonstrate that hyperinsulinemia, either in the context of insulin resistance or in response to systemic PI3K inhibition, increases tumor growth of subcutaneously implanted patient-derived xenograft models through inhibition of host PI3K^{28,38,39}. Our study

extends on this observation and shows that insulin-mediated tumor growth disproportionately occurs in LM over primary tumors or other metastatic sites, in line with higher insulin levels in the liver. These effects could be abrogated by reducing the insulin gradient between the liver and other organs through systemic delivery of insulin. Furthermore, combination of systemic PI3K inhibition with either inhibition of SGLT2 or a ketogenic diet could disrupt the effects of host-mediated increase in insulin levels and reduce LM while having little or no effect on lung metastasis burden. These findings have potential clinical relevance in specific disease contexts. For example, patients with hormone receptor-positive breast cancer, for which PI3K inhibitor alpelisib is FDA approved and ongoing studies test the benefit of adding SGLT2 inhibition or a ketogenic diet (NCT05090358), may particularly benefit from such strategies when LMs are present. Although activating mutations of *PIK3CA* are frequent in breast cancer and serve as the basis for the use of PI3K inhibitors in breast cancer, our study suggests that this oncogenic dependency may not be necessary to select patients toward PI3K inhibitor-based combination treatment strategies, thus expanding the potential pool of patients who may benefit from such therapies.

Our study has potential limitations: First, loss or reduced expression of *Pip4k2c* likely represents one example of resulting hypersensitization to insulin and may have effects beyond regulation of this pathway that we did not measure^{40,41}. Our initial screen only targeted kinases; thus, more extensive unbiased approaches are necessary to characterize the entire landscape of potential drivers of LM development. Second, analysis of human data showed that *PIK3CA* mutations are infrequent in melanoma but enriched in melanoma LM, suggesting that genomic activation of the pathway may directly drive LM in a portion of patients, independent from regulation by *Pip4k2c* or its isoforms. Importantly, even in the presence of *PIK3CA* mutations, insulin is still required to activate the pathway. Third, transcriptomics analyses of human data may suffer from contamination by normal hepatocytes in LM and respective parenchymal and infiltrating cells in other analyzed organ sites. However, it is unlikely that this factor had a major effect, as we observed similar pathway enrichment in mouse metastases profiled by single-cell RNA-seq, where analyses were restricted to malignant cells. Lastly, further work is required to determine the role of niche cells and the tumor-microenvironment in liver-metastatic organotropism.

Methods

Ethics statement

The research performed in this study complies with ethical regulations. Human specimen research was approved by the Institutional Review Board at Columbia University Irving Medical Center (#AAO5706). All mouse experiments were performed under Institutional Animal Care and Use Committee-approved animal protocols at Columbia University (AABE6570) and Harvard Medical School (AABQ9616). The maximum subcutaneous tumor size permitted by both Institutional Animal Care and Use Committees is 20 mm and was never exceeded. Source data are provided for all in vivo experiments.

Mice

6- to 8-week-old C57BL/6J (Charles River: 027), NOD/SCID/IL2rgR (NSG) (JAX: 005557) and/or BALB/c (JAX: 000651) female mice were obtained from Charles River and/or Jackson laboratories. Mice received a normal chow diet (PicoLab, Rodent 20 5053 laboratory diet) or a ketogenic diet (Thermo Fisher, AIN-76A) where indicated, with free access to drinking water. Diet composition is described in Supplementary Table 7. Mice were housed under pathogen-free conditions. Sex was not considered in the study design.

Cell culture

Mouse melanoma cell line HcMel12 was kindly provided by T. Tüting (Magdeburg, Germany). Melanoma cells were grown in complete

RPMI-1640 medium (Gibson Bioscience) as described previously¹³. RPMI 1640 supplemented with 10% FBS (Gibco, 10437028), 10 mM non-essential amino acids, 1 mM HEPES (all from Life Technologies) and 20 μ M 2-mercaptoethanol (Sigma). Mouse colorectal carcinoma cell line CT26 was cultured in RPMI 1640 medium supplemented with 10% FBS. A375 and HEK293 cells were purchased from ATCC and grown in DMEM supplemented with 10% FBS. Cell lines were routinely tested for mycoplasma contamination using Lonza MycoAlert Kit (LT07-318).

Generation of a Cas9-expressing HcMel12 melanoma cells

Cas9 lentivirus was generated from HEK-293T cells transfected with pLX-31Cas9v.2 plasmids (Addgene, 118018) and packaging plasmids pMD2.G (Addgene, 12259) and psPAX2 (Addgene, 12260) using TransIT-LT1 Transfection reagent (Mirus). HcMel12 melanoma cells were transduced with Cas9 lentiviral particles followed by blasticidin selection (1 μ g ml⁻¹) for 48 h. To assess Cas9 cutting efficiency in HcMel12-Cas9-expressing cells, cells were transduced with lentivirus expressing EGFP (pXPR_011 (Addgene, 59702; gift from J. Doench and D. Root)) and EGFP-targeting sgRNA. Cas9 activity was estimated based on the fraction of EGFP-negative cells 7 days later using FACS Canto flow cytometry (BD Biosciences) and analyzed with FlowJo software (TreeStar, v10 for Mac). The fraction of EGFP-negative cells was used to estimate Cas9 efficiency.

Propagation of kinome sgRNA libraries and lentivirus production

Mouse kinome CRISPR knockout library (Brie) was purchased from Addgene (Addgene, 75316) and includes 2,852 sgRNAs targeting 713 kinase genes and 100 control non-targeting sgRNAs (Supplementary Table 3). For library production, HEK-293T cells were seeded in DMEM + 10% FBS in T175 flasks 1 day prior. At 80% confluency, cells were transfected with the Brie library and the packaging/envelope plasmids pMD2.G (Addgene, 12259) and psPAX2 (Addgene, 12260) using TransIT-LT1 Transfection reagent (Mirus). After 6 h, media was replaced with DMEM + 20% FBS, and virus was collected after 48 h, filtered and stored at -80 °C.

In vivo CRISPR-Cas9 screen

HcMel12-Cas9 melanoma cells were transduced at a multiplicity of infection < 0.1 with Brie lentivirus at $\geq 1,000$ cells/construct per infection replicate ($\sim 3 \times 10^7$ pre replicate). Cells were spin-infected at 1,000g, 37 °C for 2 h and incubated for 16 h followed by a media change. On day 2 after transduction, the cells were put into Blasticidin selection (1 μ g/ml) for 7 days and Puromycin (1 μ g/ml) for the remainder of the experiment. On day 14, 3×10^6 of library-transduced HcMel12-Cas9 cells were injected into the right flank or lateral via tail vein of the mice. In parallel cells were kept in culture for 21, 28, 35, 42, 49 and 52 days. Tumor growth and signs of sickness were monitored over time. Mice were euthanized after 4 weeks and tumors and mice were evaluated for metastasis presence, lesions were dissected for gDNA isolation, sgRNA amplification, and sequencing. Genomic DNA was extracted using Qiagen DNeasy Blood & Tissue Kit (Qiagen, 69506). sgRNA amplification and sequencing library construction were performed as described previously¹⁵, and sgRNA library was sequenced on a Illumina HiSeq2500 Instrument. CRISPR-Cas9 screens were analyzed and visualized using software packages MAGeCK and MAGeCKFlute R (v4.0.3)⁴².

Generation of KO, knockdown and gene-overexpressing cell lines

Individual tumor cell KOs were generated using Cas9 ribonucleoproteins nucleofection as described previously⁴³. Target sequences were designed using CHOP-CHOP tool (<https://chopchop.cbu.uib.no>) or sequences were derived from the original kinome library (sequence information in Supplementary Table 8). For insulin receptor knockdown experiments dox-inducible shRNA was used

as described previously²⁸ (Sequence information in Supplementary Table 8). For generation of miR-E shRNAs, 97-mer oligonucleotides were purchased coding for predicted shRNAs using Splash RNA, <http://splashrna.mskcc.org/>. Oligonucleotides were PCR amplified using the primers miRE-Xho-fw (5'-TGAAGCTCGAGAAGGTATATTCGCTGTTGACA GTGACCG-3') and miRE-Eco-rev (5'-TGAAGCTCGAGAAGGTATATTCGCTGTTGACAGTGACCG-3'). To generate full-length and N-terminal mutant *Pip4k2c* overexpression constructs, open reading frames were cloned into pLX305 using Gateway cloning (Supplementary Table 8). Human pDONR223-PIP5K2C (Addgene, 23450) and N-terminal mutant human *PIP4K2C*, ORF were cloned into pLX307 using Gateway cloning and Gibson cloning, respectively. All vectors were sequence verified using Sanger sequencing followed by whole plasmid sequencing.

Proliferation assay

1,000 cells were seeded in 96-well plates. After 1, 2 or 3 days of proliferation, cells were fixed in 4% PFA and stained with DAPI. Timepoint zero was used as a reference control. Images were acquired on IVOS microscope, and analysis was performed using Cell Profiler software (<https://cellprofiler.org>).

Transwell migration assay

Migration was assessed using transwell assays. 2×10^4 melanoma cells pretreated with insulin were placed in the upper compartment of a transwell chamber with 8.0 μm pore size (Corning, 3422) containing 300 μl (top) and 700 μl media in the lower chamber. Cells were led to adhere and transmigrate through the membrane at 37 °C 5% CO₂. Wells treated with no insulin served as controls. After 16 h, transmigrated cells on the lower surface of the membrane were stained with CFSE and fixed with 4% paraformaldehyde, and the mean number was counted in five high-power fields using Inverted Microscope (Olympus).

Immunoblots

Cells were lysed in 1x Laemmli buffer (10,000 cells μl^{-1}) followed by 5 min incubation at 95 °C. Lysates were separated by 10% SDS-gel electrophoresis and transferred to a PVDF membrane (Thermo Fisher, IB24001). Membranes were blocked for 1 h (Roche, 11921673001 blocking buffer) in Tris-buffered saline, pH 7.6 (Agilent Technologies, S196830-2) and probed with primary antibodies overnight at 4 °C followed by 1 h incubation in secondary antibodies at room temperature. Proteins were detected using the Odyssey CLx Imaging system (LI-COR Biosciences). Antibody information is provided in the Reporting Summary. Membranes were stripped using Stripping Buffer (Thermo Fisher, 46430). Full blots corresponding to the immunoblots shown in the main and supplementary figures are provided as a source file.

RNA isolation, RNA-seq and analysis

2×10^6 parental and *Pip4k2c*^{KO} HcMel12 melanoma cells were plated in 6-well plates in FBS-free media overnight, with three biological replicates per condition (total of 12 samples). The next day, cells were treated with insulin (125 ng ml⁻¹) for 4 h (Supplementary Table 4). RNA was extracted using Qiagen kit (74136) and sequenced on a HiSeq2500 (Illumina). Transcripts were quantified with Salmon⁴⁴ using the mouse reference genome release GRCh38.97. The tximeta R package (v.4.3)⁴⁵ was used to import transcript-level counts and aggregate them by gene. DESeq2 package was applied to generate normalized gene counts. GSEA for pathway genes was identified using BROAD java GSEA software with normalized gene counts as input (<https://www.gsea-msigdb.org/gsea/index.jsp>).

In vitro drug treatment

Cells were washed 1x in PBS, placed in FBS-free media overnight and treated for 1 h with PI3K inhibitors (Pictilisib/GDC-0941 (S1065) and Alpelisib (S2814) from Selleck Chemicals) as indicated with insulin for 15 min before collection for immunoblotting. To induce insulin receptor

knockdown cells were treated with 1 $\mu\text{g ml}^{-1}$ dox (Sigma, D9891-5G) for 48 h, washed once with PBS and subjected to signaling studies.

Animal metastasis and drug treatment studies in vivo

5×10^5 HcMel12 mouse melanoma cells and 1×10^5 A375 human melanoma cells were injected into the lateral tail vein. Mice were monitored over 3–4 weeks. When mice showed signs of sickness, 20% of weight loss, impaired activity, hunching and limb paralysis, animals were euthanized, and organs were harvested for evaluation on metastasis presence. For in vivo drug treatment studies, Pictilisib (GDC-0941, HY-50094) and Canagliflozin (JNJ 28431754, HY-10451) were purchased from Medchem Express. The day after tumor cell injection, mice were given vehicle control or treated (daily, 5 out of 7 days) with GDC-0941 (100 mg kg⁻¹) or SGLT2i (6 mg kg⁻¹) prepared in 'CMC' solution (0.5% carboxy-methyl-cellulose sodium (Sigma, C9481-500G) in distilled water supplemented with 0.2% Tween-80 (Sigma, BCBW1801)) for the duration of the experiment unless otherwise stated. To maintain *Insr* knockdown in vivo, mice bearing *Pip4k2c*^{KO} cells with dox-inducible *Insr* shRNA were administered 3 mg kg⁻¹ dox (Sigma, D3072) intraperitoneally daily for 3–4 weeks. Ketogenic diet was started 10 days before tumor cell injection where indicated. In experiments combining GDC-0941 and SGLT2 inhibitor (Canagliflozin), the latter was administered 60 min before GDC-0941²⁸ administration. 2×10^5 tumor cells were injected subcutaneously, and tumor growth was monitored over time. When tumors were palpable, mice were treated with GDC-0941 (100 mg kg⁻¹) alone or in combination with SGLT2i (6 mg kg⁻¹) three times a week until the end of the experiment. Mice were euthanized, and tumor growth was evaluated.

Endoscopy-guided orthotopic tumor transplantation and injections

Orthotopic injections of CT26 cells was performed as described previously⁴⁶. Briefly, cell lines were split 2 days prior. On the day of injection, cells at 80–90% confluency were harvested by TrypLE Express enzyme (Gibco, 12604013). Tumor cells were resuspended in PBS + 10% Matrigel at 2×10^6 ml⁻¹. 100 μl was injected into the colon submucosa of each BALB/c recipient mouse by optical colonoscopy using a Hamilton syringe (7656-1) and a custom 33 G needle (Hamilton, custom made similar to 7803-05, 16", Pt 4, Deg 12). Successful injections were confirmed by observing large bubbles in the colon mucosa. After 14 days mice were euthanized and organs evaluated for metastasis presence. Optical colonoscopy was performed 2 weeks later to assess tumor formation using a Karl Storz Image 1 HD Camera System, Image 1 HUB CCU, 175-Watt Xenon Light Source, and Richard Wolf 1.9 mm/9.5 Fr Integrated Telescope (part number 8626.431). One injection was performed per mouse.

Implantation of insulin pads in NSG mice

NSG mice were implanted with 2×3 mm slow-release insulin pellets (LinBit, LinShin) on the dorsum under the skin. Under isoflurane anesthesia, mice were shaved, the surface of the skin treated with a 70% isopropyl alcohol and a lidocaine-based cream (for example, Emla). The insulin pellet was inserted using 12 G trocar and the skin opening is sealed with a drop of Vetbond. After 1 day, 1×10^5 tumor cells were injected via lateral tail vein, and tumor metastatic burden was evaluated after 4 weeks.

Blood glucose, C-peptide and tissue insulin measurements

10 μl blood was taken from the tail of mice before treatment and at indicated time points (15, 30, 60, 90, 120, 180 and 240 min) and blood glucose was measured using a Prodigy AutoCode Glucometer. At the end point, >100 μl blood was drawn from the mice into heparin-coated tubes (Stem Cell Technologies, 07980). Blood was centrifuged (10,000g for 10 min at 4 °C), and plasma was stored at -80 °C. Mouse and human C-peptide levels in plasma and mouse insulin levels in liver

and lung tissue were measured using commercial ELISA kits (Mouse C-peptide ELISA: 80-CPTMS-E01 (ALPCO); STELLUX Chemiluminescence Human C-peptide ELISA: 80-CPTHU-CH01 (ALPCO); Insulin: Invitrogen, EMINS).

Tissue collection

Liver and lung tissue was collected immediately after mice were killed and snap-frozen in liquid nitrogen. For tissue protein isolation, 5 mg powdered liver and lung tissue were homogenized in 300 μ l Mammalian Protein Extraction Reagent (78501) buffer with proteinase inhibitors (1861281) and incubated at 4 °C for 2 h with rotating, followed by a 20-min spin at 20,000 g, 4 °C. Supernatant was collected and stored at –80 °C.

FDG-PET

C57/BL6 mice were injected with *Pip4k2c*^{KO} melanoma cells. After 3 weeks, mice were scanned for LM presence using PET with FDG tracer. At the time of peak blood insulin feedback (60 min after GDC-0941 injection), animals were injected intravenously with FDG. 60 min later, mice were placed into a four-mouse bed, and 30-min static PET images were acquired using a PET scanner (Siemens) followed by micro CT (MILabs) on the same bed for anatomical references. Regions of interests were manually drawn over metastases. All PET images were reconstructed using the 3D-OSEM algorithm with three iterations in 256 \times 256 matrix (Inveon) and analyzed using VivoQuant ver 4 (Invivo).

scRNA-seq

C57/BL6 mice were injected with 5 \times 10⁵ HcMel12 melanoma cells via lateral tail vein and euthanized after 21 days, with organs harvested and evaluated for metastases presence (Supplementary Table 4). Approximately 1 \times 10⁴ cells per channel were loaded on a Chromium controller (10x Genomics). Sequencing libraries were prepared using standard protocols, and libraries were sequenced on a NovaSeq with S4 flow cell (Illumina) and 2 \times 100 bp paired-end reads.

Single-cell computational analyses

Preprocessing, cell selection and filtering of individual scRNA-seq samples. Cell Ranger (v6.0.2) was used to construct a count matrix from raw reads by demultiplexing samples, aligning to refdata-gex-mm10-2020-A, processing barcodes, and collapsing reads with the same unique molecular identifier, cell barcode and gene annotation. This matrix was then imported into scanpy⁴⁷ (v1.7.2) for sample demultiplexing and analysis. 38 redundant genes were combined by summing the molecule counts. Several filtering steps within each sample were performed to ensure high data quality. Viable cells were determined based on library size (total molecule counts). Specifically, cells were ranked by library size in descending order, the normalized cumulative sum was computed based on the average of a 10-cell rolling window, and the inflection point was identified using the second derivative. All cells with a library size less than 0.9 \times the inflection point were discarded (Extended Data Fig. 4a). Additionally, cells with >20% mitochondrial transcripts (Extended Data Fig. 4b), with low coverage defined by

$$\frac{\text{reads}}{\text{molecule}} < \mu \left(\frac{\text{reads}}{\text{molecule}} \right) - 2.5 \times \text{s.d.} \left(\frac{\text{reads}}{\text{molecule}} \right),$$

or with low complexity libraries (in which detected molecules align to a small subset of genes determined by at least 0.4 \times standard deviations from a linear fit) (Extended Data Fig. 4c) were discarded. Scrublet⁴⁸ was used to predict cell doublet scores using an expected doublet rate of 0.06. The filtered count matrix was normalized by library size and scaled by a constant of 10,000. The matrix was then log-transformed using: $\log_{10}(x + 0.1) - \log_{10}(0.1)$.

Merged sample library generation. After processing and filtering individual samples, 16 murine tumor samples were merged, for a total of 98,126 cells with a median library size of 2,065 transcripts each. Genes detected in fewer than 5 cells ($n = 12,621$) were excluded. Using the infection point of the smoothed doublet score distribution as a threshold, 2,520 suspected doublet cells were eliminated (2.6%), resulting in 95,606 high-quality cells expressing 19,624 genes with 3,739 highly variable genes. Cell library size and mitochondrial content were consistent across samples (Extended Data Fig. 4d). CellAssign was used to identify tumor cells based on cell type-specific markers, revealing 1,227 tumor cells ($n = 1,124$ liver and $n = 103$ lung metastasis cells) (Extended Data Fig. 4e). Tissue-specific cell type-marker genes were assembled using the Mouse Cell Atlas⁴⁹ and Human Cell Lung Atlas⁵⁰ (described and annotated in Supplementary Table 5) and supplemented by canonical markers curated from the literature (for example, *Ngfr* for basal cells⁵¹, *Scgb1a1* for secretory/club cells⁵² and pigmentation-associated genes *Mitf*, *Mlana*, *Dct*, *Tyr* and *Tyrp1* to distinguish melanoma cells⁸).

Data visualization. Tumor cells and marker genes were visualized using UMAP in scanpy⁴⁷ after selecting 34 principal components, based on the plateau of the cumulative explained variance, and the default $k = 15$ nearest neighbors (Extended Data Fig. 4e). To compare transcriptional states in the liver and lung metastases, differential gene analysis was performed using Seurat (4.1.1)⁵³ Wilcoxon rank-sum test for differential gene expression with Bonferroni correction (Extended Data Fig. 4f). To detect biological processes associated with the tumor cells from each metastatic site, GSEA of MSigDB⁵⁴ pathways was performed (Hallmark genes, KEGG, Gene Ontology Biological Process and Wikipathways) via ClusterProfiler (v3.16.1)⁵⁵ for all differentially expressed genes (DEGs) ranked by $-\log_{10}(pval) * \text{sign}(avg_log2FC)$ (Extended Data Fig. 4e).

Bulk RNA-seq

RNA was extracted from 15 human LM samples (Supplementary Table 4). Tumor areas were macro-dissected, and RNA was extracted using Qiagen kit All Prep DNA/RNA FFPE Kit (Catalog Number 80234), quantified using Qu-bit and stored at –80 °C until use.

Poly-A pull-down was used to enrich mRNAs from total RNA samples, followed by library construction using Illumina TruSeq chemistry. Libraries were then sequenced using an Illumina NovaSeq 6000 at Columbia Genome Center. Samples were multiplexed in each lane, which yielded targeted number of paired-end 100 bp reads for each sample. RTA (Illumina) was used for base calling and bcl2fastq2 (v2.19) for converting BCL to fastq conversion, coupled with adaptor trimming. Pseudoalignment to a kallisto index created from Human transcriptomes GRCh38 was performed using kallisto (0.44.0)⁵⁶. This process resulted in 15 LM (LM15) samples. The data were combined with the MET500 effort³⁰. The MET500 RNA-seq data and sequencing sample metadata were downloaded from [https://xenabrowser.net/datapages/?cohort=MET500%20\(expression%20centric\)](https://xenabrowser.net/datapages/?cohort=MET500%20(expression%20centric)) on 2022-07-21. The MET500 fragments per kilobase of transcript per million mapped reads values were converted to transcripts per million (TPM) to be consistent with LM15. For main figure analyses Met500 samples were filtered to samples with annotated tumor content greater than 0.5. This filter increased to 0.7 for extended data figure analyses. The 0.5 cutoff led to 237 Met500 samples, including 93 liver, 16 lung and 159 non-liver metastases, whereas the 0.7 led to 141 Met500 samples, including 56 liver, 9 lung and 100 non-LMs (Supplementary Table 5). The MET500 and LM15 TPM matrix were combined, keeping genes that existed within both datasets. The MET500 samples and LM15 samples were integrated using ComBat-seq⁵⁷. This process was followed by dimensional reduction using PCA to ensure proper integration. Only genes characterized as ‘protein_coding’ were included, using biomaRt to download Ensembl biotype annotations. Genes that were nonzero in 25% or more of samples were excluded, resulting in 17,281 genes for downstream testing. DEGs were found by running a Wilcoxon rank-sum

test (`wilcox.test()` function in R) on the expression between comparison groups. GSEA was performed using `fgsea`⁵⁸ on the list of DEGs ranked by $-\log_{10}(\text{fdr}) \times \text{sign}(\log_2 \text{fold_change})$. Gene sets of interest included Cancer Hallmarks gene sets from MSigDB and KEGG, along with select pathways from WikiPathways and Gene Ontology Biological Process^{54,59,60}.

Arriaga dataset analysis. For validation of these results in a separate NPK^{EXFP} mouse model, bulk RNA-seq data from the Arriaga et al. cohort²⁹ was used. All available data from liver ($n = 7$), lung ($n = 14$) and bone metastases ($n = 15$) and primary tumors (prostate, $n = 22$) were analyzed. For differential expression analysis, raw count data was input in DESeq2. GSEA was performed using the same methods and gene sets as previously described.

Exome/RNA-seq and analysis through Caris Life Sciences

Next-generation sequencing was performed on genomic DNA isolated from microdissected formalin-fixed paraffin-embedded (FFPE) tumor samples using the NextSeq or NovaSeq 6000 platforms (Illumina). For NextSeq sequenced tumors, a custom-designed SureSelect XT assay enriched 592 whole-gene targets (Agilent Technologies). NovaSeq whole exome-sequenced tumors utilized a hybrid pull-down panel of baits targeting over 700 clinically relevant genes at high coverage, along with another panel enriching for additional >20,000 genes at a lower depth. A 500 Mb SNP backbone panel (Agilent Technologies) aided gene amplification/deletion measurements. All variants were detected with >99% confidence, an average sequencing depth of coverage of >500 and an analytic sensitivity of 5%. This test has a sensitivity to detect as low as approximately 10% population of cells containing a mutation in all exons from the high read-depth clinical genes and 99% of all exons in the 20 K whole-exome regions. Genetic variants identified were interpreted by board-certified molecular geneticists and categorized as ‘pathogenic,’ ‘likely pathogenic,’ ‘variant of unknown significance,’ ‘likely benign,’ or ‘benign,’ according to the American College of Medical Genetics and Genomics standards. When assessing mutation frequencies of individual genes, ‘pathogenic,’ and ‘likely pathogenic’ were counted as mutations, whereas ‘benign,’ ‘likely benign’ variants, and ‘variants of unknown significance’ were excluded. Variants detected were mapped to reference genome (hg19), and bioinformatics tools (BWA, SamTools, GATK and `snppF`) were used for variant calling; germline variants were filtered using databases such as 1,000 genome and dbSNP.

Tumor-specific RNA was extracted from microdissected FFPE specimens with at least 10% tumor content using a Qiagen RNeasy FFPE Kit. RNA quality and quantity were determined using the Agilent TapeStation. Biotinylated RNA baits were hybridized to the synthesized and purified cDNA targets, and the bait-target complexes were amplified in a post-capture PCR reaction. Whole transcriptome sequencing on Illumina NovaSeq 6500 generated an average of 60 M reads. Raw data was demultiplexed by Illumina Dragen BioIT accelerator, trimmed and counted, PCR duplicates were removed, and data were aligned to human reference genome hg19 by STAR aligner (v.2.7.8a). TPMs were calculated with Salmon expression pipeline. DEGs were determined by calculating \log_2 fold change between defined groups, and genes were considered significantly different when adjusted $P < 0.05$. Significantly enriched pathways across disease sites were determined using GSEA to calculate normalized enrichment score and significance level adjusted for multiple hypothesis testing⁶⁰.

Tissue metabolomics

6- to 8-week-old NSG mice were injected via tail vein with 1×10^5 A375 human melanoma cells ($n = 5$ mouse per group). Mice were monitored over 3–4 weeks. When mice showed signs of sickness, animals were euthanized, and organs were harvested for evaluation of metastases presence. Liver and lung metastases were snap frozen and subjected to downstream analysis.

Extraction. Metabolites were extracted from 50 mg frozen tissue using a two-step liquid method similar to that described by Sellik et al.⁶¹. Internal standards (¹³C₆-L-arginine, ¹³C₃ L-valine, ¹³C₂-citric acid, ²H₄-succinic acid and ¹³C₆-fructose-6-phosphate) were added, followed by homogenization, sonication and centrifugation. Supernatants were collected, dried and resuspended.

Liquid chromatography–mass spectrometry (LC-MS) analysis.

Chromatographic separation utilized Agilent 1290 Infinity II Bio LC system with an AdvanceBio MS Spent Media (150 × 2.1 mm, 2.7 μm). The elution used a gradient at a flow rate of 250 μl min⁻¹ with water (10 mM ammonium acetate, pH 9) as solvent A and acetonitrile/water (90/10; v/v; 10 mM ammonium acetate, pH 9) as solvent B. The linear gradient was: 0 min, 90% B; 2 min, 90% B; 12 min, 40% B; 13 min, 20% B; 16 min, 20% B; followed by 9 min for re-equilibration. Column temperature was maintained at 35 °C, and sample injection volume was 5 μl.

Mass spectrometric detection was facilitated by coupling the LC system with a Thermo Orbitrap Q Exactive. Ionization in positive and negative modes utilized the HESI II ion source. MS parameters were optimized, with scan ranges of 70–1,050 m/z and 70,000 resolution in full scan mode and 17,500 resolution for data-dependent MS2 acquisitions.

Data analysis. LC-MS data were processed with MS-Dial, using accurate mass and MS2 spectra for compound identification. MS-DIAL metabolomics MSP spectral libraries were employed for identification. For nontargeted analysis, compounds underwent statistical analysis using MetaboAnalyst. Pareto scaling, univariate and multivariate statistical methods (PCA and PLS-DA) and data normalization.

Specifically for TCA cycle and glycolysis compounds, suspected target analysis was conducted. LC-MS data were manually integrated using Skyline, identifying peaks based on accurate mass and MS2 spectra. The peak areas were normalized using ¹³C₂-citric acid as an internal standard.

Statistical analysis

Graphs represent mean ± s.e.m. unless otherwise stated. Statistical analyses were carried out using GraphPad Prism 9 Software (GraphPad Software). Results were considered statistically significant when $P < 0.05$ and precise significance levels are indicated for respective comparisons. The figure legends specify the statistical tests used for each data along with the corresponding sample size (n). In the graphs, individual data points are depicted as dots. To account for multiple comparisons, appropriate adjustments were applied as detailed in the figure legends. No statistical methods were used to predetermine the sample size. Sample sizes were instead determined based on historical sample sizes capable of detecting biologically significant differences for certain assays. If no historical data were available, pilot experiments were performed to determine the relative variability of the assay. Data were assumed to be normal, but this was not always formally tested. No data were excluded from analysis. No randomization was performed in the conducted experiments. No sex or gender analysis was carried out. Data collection and analysis were not performed blind to the conditions of the experiments and outcome assessment.

Reporting summary

Further information on research design is available in the Nature Portfolio Reporting Summary linked to this article.

Data availability

Gene expression data generated in this study have been deposited in the Gene Expression Omnibus under accession number [GSE188391](https://www.ncbi.nlm.nih.gov/geo/query/acc.cgi?acc=GSE188391). Previously published RNA-seq data for the Arriaga et al. cohort are accessible under accession number [GSE143812](https://www.ncbi.nlm.nih.gov/geo/query/acc.cgi?acc=GSE143812), and MET500 data are

accessible at [https://xenabrowser.net/datapages/?cohort=MET500%20\(expression%20centric\)](https://xenabrowser.net/datapages/?cohort=MET500%20(expression%20centric)).

The deidentified DNA-sequencing and RNA-seq data are owned by Caris Life Sciences and cannot be publicly shared due to the data usage agreement signed by B. Izar at Columbia University Irving Medical Center. Qualified researchers can apply for access to these data by contacting J. Xiu (jxiu@carisls.com), submitting a brief proposal and signing a data usage agreement. Metabolomics data have been deposited in the Metabolomics Workbench (the NIH Common Fund's National Metabolomics Data Repository website, <https://www.metabolomicsworkbench.org>) under study ID ST002851 and can be accessed directly via its project ID (<https://doi.org/10.21228/M8043D>).

The remaining data are available within the article or as source data. Source data are provided with this paper.

Code availability

No custom algorithms were used in this study.

References

- Chaffer, C. L. & Weinberg, R. A. A perspective on cancer cell metastasis. *Science* **331**, 1559–1564 (2011).
- Gao, Y. et al. Metastasis organotropism: redefining the congenial soil. *Dev. Cell* **49**, 375–391 (2019).
- Tsilimigras, D. I. et al. Liver metastases. *Nat. Rev. Dis. Primers* **7**, 27 (2021).
- Lee, J. C. et al. Regulatory T cell control of systemic immunity and immunotherapy response in liver metastasis. *Sci. Immunol.* **5**, eaba0759 (2020).
- Tumeh, P. C. et al. Liver metastasis and treatment outcome with anti-PD-1 monoclonal antibody in patients with melanoma and NSCLC. *Cancer Immunol. Res.* **5**, 417–424 (2017).
- Bergers, G. & Fendt, S.-M. The metabolism of cancer cells during metastasis. *Nat. Rev. Cancer* **21**, 162–180 (2021).
- Priestley, P. et al. Pan-cancer whole-genome analyses of metastatic solid tumours. *Nature* **575**, 210–216 (2019).
- Biermann, J. et al. Dissecting the treatment-naïve ecosystem of human melanoma brain metastasis. *Cell* **185**, 2591–2608 (2022).
- Broadfield, L. A. et al. Fat induces glucose metabolism in nontransformed liver cells and promotes liver tumorigenesis. *Cancer Res.* **81**, 1988–2001 (2021).
- Moris, D., Lu, L. & Qian, S. Mechanisms of liver-induced tolerance. *Curr. Opin. Organ Transplant.* **22**, 71–78 (2017).
- Lee, J. W. et al. Hepatocytes direct the formation of a pro-metastatic niche in the liver. *Nature* **567**, 249–252 (2019).
- Landsberg, J. et al. Autochthonous primary and metastatic melanomas in Hgf-Cdk4 R24C mice evade T-cell-mediated immune surveillance. *Pigment Cell Melanoma Res.* **23**, 649–660 (2010).
- Bald, T. et al. Ultraviolet-radiation-induced inflammation promotes angiotropism and metastasis in melanoma. *Nature* **507**, 109–113 (2014).
- & Rogava, M. et al. Tumor cell intrinsic Toll-like receptor 4 signaling promotes melanoma progression and metastatic dissemination. *Int. J. Cancer* **150**, 142–151 (2021).
- Doench, J. G. et al. Optimized sgRNA design to maximize activity and minimize off-target effects of CRISPR-Cas9. *Nat. Biotechnol.* **34**, 184–191 (2016).
- Zaretsky, J. M. et al. Mutations associated with acquired resistance to PD-1 blockade in melanoma. *N. Engl. J. Med.* **375**, 819–829 (2016).
- Bakhoun, S. F. et al. Chromosomal instability drives metastasis through a cytosolic DNA response. *Nature* **553**, 467–472 (2018).
- Brogard, J., Zhang, Y.-W., Puto, L. A. & Hunter, T. Cancer-associated loss-of-function mutations implicate DAPK3 as a tumor-suppressing kinase. *Cancer Res.* **71**, 3152–3161 (2011).
- Chen, S. et al. Genome-wide CRISPR screen in a mouse model of tumor growth and metastasis. *Cell* **160**, 1246–1260 (2015).
- LaLonde, D. P., Brown, M. C., Bouverat, B. P. & Turner, C. E. Actopaxin Interacts with TESK1 to Regulate Cell Spreading on Fibronectin. *J. Biol. Chem.* **280**, 21680–21688 (2005).
- Yang, C.-S. et al. The protein kinase C super-family member PKN is regulated by mTOR and influences differentiation during prostate cancer progression. *Prostate* **77**, 1452–1467 (2017).
- Yang, M. et al. MYLK4 promotes tumor progression through the activation of epidermal growth factor receptor signaling in osteosarcoma. *J. Exp. Clin. Cancer Res.* **40**, 166 (2021).
- Cunningham, J. T., Moreno, M. V., Lodi, A., Ronen, S. M. & Ruggero, D. Protein and nucleotide biosynthesis are coupled by a single rate-limiting enzyme, PRPS2, to drive cancer. *Cell* **157**, 1088–1103 (2014).
- Wang, D. G. et al. PIP4Ks suppress insulin signaling through a catalytic-independent mechanism. *Cell Reports* **27**, 1991–2001 (2019).
- Kim, T. et al. *TRIB1* regulates tumour growth via controlling tumour-associated macrophage phenotypes and is associated with breast cancer survival and treatment response. *Theranostics* **12**, 3584–3600 (2022).
- Soubeyrand, S., Martinuk, A., Lau, P. & McPherson, R. *TRIB1* is regulated post-transcriptionally by proteasomal and non-proteasomal pathways. *PLoS One* **11**, e0152346 (2016).
- Lafitte, M. et al. FGFR3 has tumor suppressor properties in cells with epithelial phenotype. *Mol. Cancer* **12**, 83 (2013).
- Hopkins, B. D. et al. Suppression of insulin feedback enhances the efficacy of PI3K inhibitors. *Nature* **560**, 499–503 (2018).
- Arriaga, J. M. et al. A MYC and RAS co-activation signature in localized prostate cancer drives bone metastasis and castration resistance. *Nat. Cancer* **1**, 1082–1096 (2020).
- Robinson, D. R. et al. Integrative clinical genomics of metastatic cancer. *Nature* **548**, 297–303 (2017).
- Sridhar, S. et al. Prognostic significance of liver metastasis in durvalumab-treated lung cancer patients. *Clinical Lung Cancer* **20**, e601–e608 (2019).
- Tumeh, P. C. et al. Liver metastasis and treatment outcome with anti-PD-1 monoclonal antibody in patients with melanoma and NSCLC. *Cancer Immunol. Res.* **7**, 282 (2017).
- Birkbak, N. J. & McGranahan, N. Cancer genome evolutionary trajectories in metastasis. *Cancer Cell* **37**, 8–19 (2020).
- El-Kebir, M., Satas, G. & Raphael, B. J. Inferring parsimonious migration histories for metastatic cancers. *Nat. Genet.* **50**, 718–726 (2018).
- Sivanand, S. et al. Cancer tissue of origin constrains the growth and metabolism of metastases. Preprint at *bioRxiv* <https://doi.org/10.1101/2022.08.17.504141> (2022).
- Yu, J. et al. Liver metastasis restrains immunotherapy efficacy via macrophage-mediated T cell elimination. *Nat. Med.* **27**, 152–164 (2021).
- Reichert, M. et al. Regulation of epithelial plasticity determines metastatic organotropism in pancreatic cancer. *Dev. Cell* **45**, 696–711 (2018).
- Kalaany, N. Y. & Sabatini, D. M. Tumours with PI3K activation are resistant to dietary restriction. *Nature* **458**, 725–731 (2009).
- Nencioni, A., Caffa, I., Cortellino, S. & Longo, V. D. Fasting and cancer: molecular mechanisms and clinical application. *Nat. Rev. Cancer* **18**, 707–719 (2018).
- Zhang, Y. et al. C24-ceramide drives gallbladder cancer progression through directly targeting phosphatidylinositol 5-phosphate 4-kinase type-2 gamma to facilitate mammalian target of rapamycin signaling activation. *Hepatology* **73**, 692–712 (2021).

41. Triscott, J. et al. PI5P4Ka supports prostate cancer metabolism and exposes a survival vulnerability during androgen receptor inhibition. *Sci. Adv.* **9**, eade8641 (2023).
 42. Wang, B. et al. Integrative analysis of pooled CRISPR genetic screens using MAGeCKFlute. *Nat. Protoc.* **14**, 756–780 (2019).
 43. Frangieh, C. J. et al. Multi-modal pooled Perturb-CITE-Seq screens in patient models define novel mechanisms of cancer immune evasion. Preprint at *bioRxiv* <https://doi.org/10.1101/2020.09.01.267211> (2020).
 44. Patro, R., Duggal, G., Love, M. I., Irizarry, R. A. & Kingsford, C. Salmon provides fast and bias-aware quantification of transcript expression. *Nat. Methods* **14**, 417–419 (2017).
 45. Love, M. I. et al. Tximeta: Reference sequence checksums for provenance identification in RNA-seq. *PLoS Comput. Biol.* **16**, e1007664 (2020).
 46. Beyaz, S. et al. High-fat diet enhances stemness and tumorigenicity of intestinal progenitors. *Nature* **531**, 53–58 (2016).
 47. Wolf, F. A., Angerer, P. & Theis, F. J. SCANPY: large-scale single-cell gene expression data analysis. *Genome Biol.* **19**, 15 (2018).
 48. Wolock, S. L., Lopez, R. & Klein, A. M. Scrublet: computational identification of cell doublets in single-cell transcriptomic data. *Cell Syst.* **8**, 281–291 (2019).
 49. Han, X. et al. Mapping the Mouse Cell Atlas by Microwell-Seq. *Cell* **172**, 1091–1107 (2018).
 50. Sikkema, L. et al. An integrated cell atlas of the lung in health and disease. *Nat. Med.* **29**, 1563–1577 (2023).
 51. Rock, J. R. et al. Basal cells as stem cells of the mouse trachea and human airway epithelium. *Proc. Natl Acad. Sci. USA* **106**, 12771–12775 (2009).
 52. Rawlins, E. L. et al. The Role of Scgb1a1⁺ Clara cells in the long-term maintenance and repair of lung airway, but not alveolar, epithelium. *Cell Stem Cell* **4**, 525–534 (2009).
 53. Stuart, T. et al. Comprehensive integration of single-cell data. *Cell* **177**, 1888–1902 (2019).
 54. Liberzon, A. et al. The Molecular Signatures Database (MSigDB) hallmark gene set collection. *Cell Syst* **1**, 417–425 (2015).
 55. Yu, G., Wang, L.-G., Han, Y. & He, Q.-Y. clusterProfiler: an R package for comparing biological themes among gene clusters. *OMICS* **16**, 284–287 (2012).
 56. Bray, N. L., Pimentel, H., Melsted, P. & Pachter, L. Near-optimal probabilistic RNA-seq quantification. *Nat. Biotechnol.* **34**, 525–527 (2016).
 57. Zhang, Y., Parmigiani, G. & Johnson, W. E. ComBat-seq: batch effect adjustment for RNA-seq count data. *NAR Genom. Bioinform.* **2**, lqaa078 (2020).
 58. Korotkevich, G. et al. Fast gene set enrichment analysis. Preprint at *bioRxiv* <https://doi.org/10.1101/060012> (2021).
 59. Kanehisa, M. & Goto, S. KEGG: Kyoto Encyclopedia of Genes and Genomes. *Nucleic Acids Res.* **28**, 27–30 (2000).
 60. Subramanian, A. et al. Gene set enrichment analysis: a knowledge-based approach for interpreting genome-wide expression profiles. *Proc. Natl Acad. Sci. USA* **102**, 15545–15550 (2005).
 61. Sellick, C. A., Hansen, R., Stephens, G. M., Goodacre, R. & Dickson, A. J. Metabolite extraction from suspension-cultured mammalian cells for global metabolite profiling. *Nat. Protoc.* **6**, 1241–1249 (2011).
- A. Hung, S.-H. Wilhelm and L. Hsiao-Yun from Columbia University for technical advice. B.I. is supported by National Institute of Health grants R37CA258829, R01CA280414, R01CA266446 and U54CA274506 and by the Pershing Square Sohn Cancer Research Alliance Award, the Burroughs Wellcome Fund Career Award for Medical Scientists, a Tara Miller Melanoma Research Alliance Young Investigator Award, the Louis V. Gerstner, Jr. Scholars Program and the V Foundation Scholars Award. B.N. was supported by K00CA234950. M. Röcken is supported by Wilhelm-Sander-Stiftung (2020.100.1); DFG RO 764 15/2; Cluster of Excellence iFIT (EXC 2180) “Image-Guided and Functionally Instructed Tumor Therapies”, University of Tübingen, Germany, funded by the Deutsche Forschungsgemeinschaft (DFG, German Research Foundation) under Germany’s Excellence Strategy EXC 2180-390900677. E.M.E. partially supported by NIH T32 (grant GM132083). L.C. is supported by NIH/NCI grant F30CA281104. S.F.B. is supported by Mark Foundation for Cancer Research (20-028-EDV), Oliver S. and Jennie R. Donaldson Charitable Trust, Mathers Foundation, CSHL Cancer Center Shared Resources (Animal and Histology Core Facilities) and acknowledges support by NCI Cancer Center Support grant P30CA045508. L.C.C. is supported by NCI R35 CA197588. This work was supported by NIH/NCI Cancer Center Support Grant P30CA013696 and MSTP training grant T32GM007367 (for MD/PHD Students). Metabolomics Workbench is supported by NIH grant U2C-DK119886 and OT2-OD030544 grants. The following illustrations were prepared using [BioRender.com](https://www.biorender.com): Fig. 1a,h, Fig. 3h and Fig. 6a.

Author contributions

B.I. conceived of and supervised the work. M. Rogava designed, performed and analyzed all key experiments. J.C.M., S.H.D., C.C., S. Tang, P.H., A.D.A., L.C., M.J.L., G.Z., B.N., S.C., R.J.C. and O.S. performed and supported experiments. M. Rogava and C.H. analyzed CRISPR screens. and in vitro RNA-seq data. T.J.A., S.K.D., S.W., C.G., S. Tagore, Y.W., W.G. and D.L. analyzed patient RNA-seq data newly generated here, assembled from publicly available data, or the Caris Life Sciences data. W.-Y.C., E.M.E. and A.M.L. analyzed scRNA-seq data. L.M., N.M., G.A., J.R., S.W.M. and A.T. generated and analyzed metabolomics data. A. Molotkov and A. Mintz performed PET-CT imaging studies. G.S., G.T.G., T.T., D.S., M. Röcken, T.K.E. and S.F.B. provided key materials, reagents or data. M.S., S.B., L.C.C., P.K.S., A.T., D.L. and A.M.L. provided additional study supervision. M. Rogava and B.I. wrote the initial and revised manuscripts with input and contributions from all authors. All authors approved the revised manuscript.

Competing interests

B.I. has received consulting fees/honoraria from Volastra Therapeutics, Merck, AstraZeneca, Eisai and Janssen Pharmaceuticals and has received research funding to Columbia University from Alkermes, Arcus Biosciences, Checkmate Pharmaceuticals, Compugen, Immunocore and Synthekine. None of these are relevant to the current work. C.G. has received consulting fees from Watershed Informatics. S.F.B. owns equity in, receives compensation from and serves as a consultant and the Scientific Advisory Board and Board of Directors of Volastra Therapeutics. L.C.C. is a co-founder, member of the scientific advisory board and holds equity in Agios, Petra, Volastra Therapeutics, Faeth and Larkspur. These companies are developing novel therapies for cancer, though drugs from these companies are not discussed in this paper. D.S. reports grants (to institution) from Amgen, Array/Pfizer, Bristol-Myers Squibb, MSD, Novartis and Roche; consulting fees/honoraria from 4SC, Amgen, Array Biopharma, AstraZeneca, Bristol-Myers Squibb, Daiichi Sankyo, Haystick, Immunocore, InFlarX, Innocent, LabCorp, Merck Serono, MSD, Nektar, NeraCare, Novartis, OncoSec, Pfizer, Philogen, Pierre Fabre, Replimune, Roche, Sandoz, Sanofi/Regeneron and Sun Pharma; support for attendings meetings or travel support from Bristol-Myers

Acknowledgements

We sincerely thank S. H. Davis, who sadly passed away during the completion of this study, for her dedication to excellence in cancer biology research and her passion for conducting humane animal research. We also thank J. Doench (genome perturbation platform at the Broad Institute) for technical guidance on the in vivo CRISPR screen, A. V. Parent from UCSF for technical advice, and E. Choi,

Squibb, MSD, Merck Serono, Novartis, Pierre Fabre and Sanofi; participation on drug safety monitoring or advisory boards for 4SC, Amgen, Array Biopharma, AstraZeneca, Bristol-Myers Squibb, Daiichi Sankyo, Immunocore, InFlarX, Merck Serono, MSD, Nektar, NeraCare, Novartis, OncoSec, Pfizer, Philogen, Pierre Fabre, Replimune, Roche, Sandoz, Sanofi/Regeneron and SunPharma; and leadership roles for DeCOG, German Cancer Society, Hiege-Stiftung, Deutsche Hautkrebsstiftung, Nationale Versorgungskonferenz Hautkrebs (NVKH) and European Melanoma Registry (EuMelaReg). S.K.D., S.W. and G.S. are employees of Caris Life Sciences. The other authors declare no competing interests.

Additional information

Extended data is available for this paper at <https://doi.org/10.1038/s43018-023-00704-x>.

Supplementary information The online version contains supplementary material available at <https://doi.org/10.1038/s43018-023-00704-x>.

Correspondence and requests for materials should be addressed to Benjamin Izar.

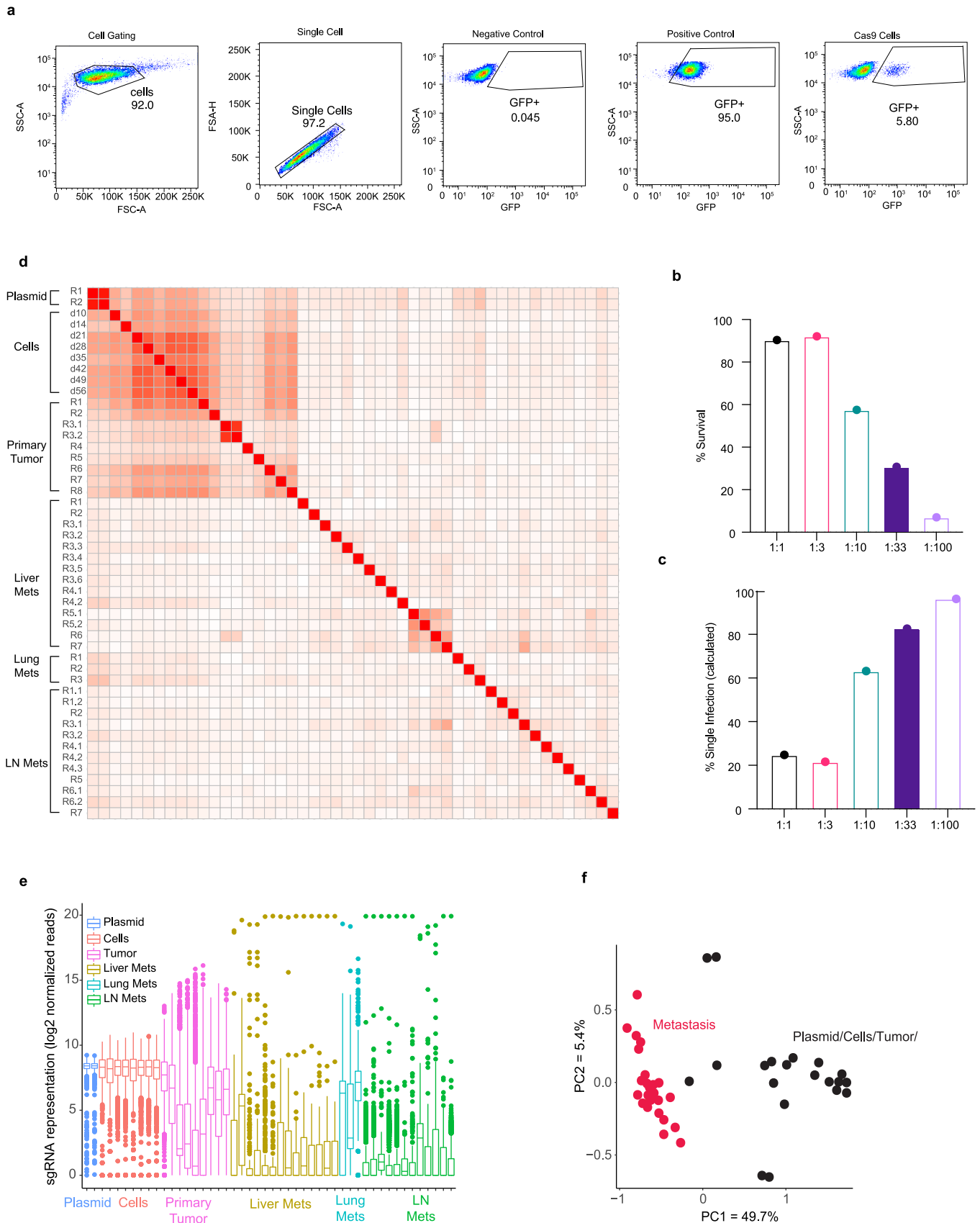
Reprints and permissions information is available at www.nature.com/reprints.

Publisher's note Springer Nature remains neutral with regard to jurisdictional claims in published maps and institutional affiliations.

Springer Nature or its licensor (e.g. a society or other partner) holds exclusive rights to this article under a publishing agreement with the author(s) or other rightsholder(s); author self-archiving of the accepted manuscript version of this article is solely governed by the terms of such publishing agreement and applicable law.

© The Author(s), under exclusive licence to Springer Nature America, Inc. 2024

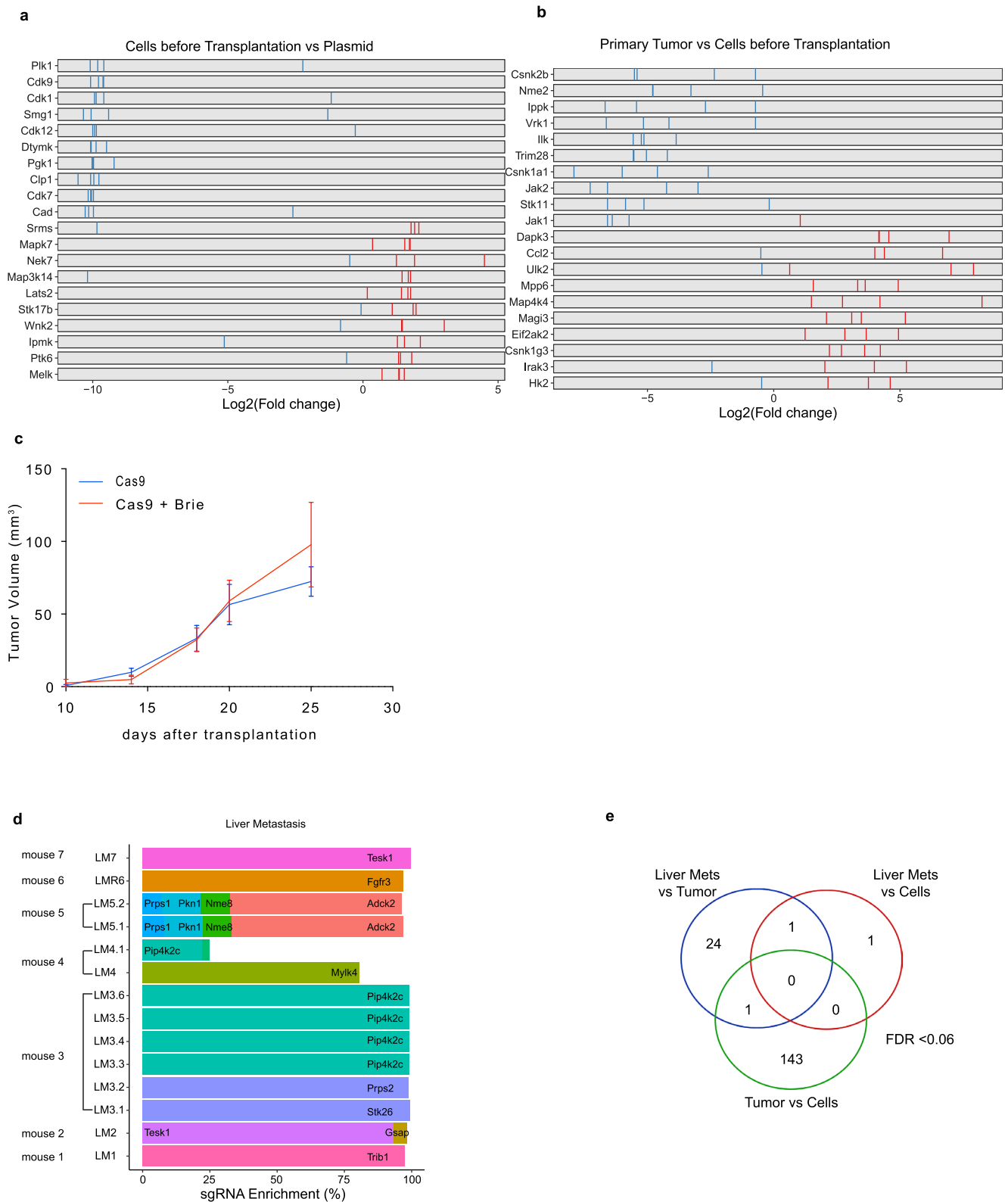
¹Division of Hematology/Oncology, Department of Medicine, Columbia University Irving Medical Center, New York, NY, USA. ²Herbert Irving Comprehensive Cancer Center, Columbia University Vagelos School of Physicians and Surgeons, New York, NY, USA. ³Columbia Center for Translational Immunology, Columbia University Irving Medical Center, New York, NY, USA. ⁴Department of Medical Oncology, Dana-Farber Cancer Institute, Boston, MA, USA. ⁵Department of Physiology, Biophysics, and Systems Biology, Weill Cornell Medicine, New York, NY, USA. ⁶Meyer Cancer Center, Weill Cornell Medicine, New York, NY, USA. ⁷Institute for Computational Biomedicine, Weill Cornell Medicine, New York, NY, USA. ⁸Laboratory for Systems Pharmacology, Harvard Medical School, Boston, MA, USA. ⁹Tri-Institutional Training Program in Computational Biology and Medicine, Weill Cornell Medicine, New York, NY, USA. ¹⁰Cold Spring Harbor Laboratory, Cold Spring Harbor, NY, USA. ¹¹Caris Life Sciences, Phoenix, AZ, USA. ¹²Program for Mathematical Genomics, Department of Systems Biology, Columbia University, New York, NY, USA. ¹³Department of Pathology and Cell Biology, Columbia University Irving Medical Center, New York, NY, USA. ¹⁴Department for Dermatology, Venerology and Allergology, University Hospital Essen, NCT West, Campus Essen, German Cancer Consortium, Partner Site Essen & University Alliance Ruhr, Research Center One Health, Essen, Germany. ¹⁵Georgetown Lombardi Comprehensive Cancer Center, Washington, DC, USA. ¹⁶Applied Analytical Chemistry, University of Duisburg-Essen, Essen, Germany. ¹⁷Laboratory for Experimental Dermatology, Department of Dermatology, University of Magdeburg, Magdeburg, Germany. ¹⁸Department of Dermatology, University Hospital Tuebingen, Tuebingen, Germany. ¹⁹Department of Dermatology, Venerology and Allergology, Charité University Hospital, Berlin, Germany. ²⁰Department of Radiology, Columbia University Medical Center, New York, NY, USA. ²¹Human Oncology and Pathogenesis Program, Memorial Sloan Kettering Cancer Center, New York, NY, USA. ²²Department of Radiation Oncology, Memorial Sloan Kettering Cancer Center, New York, NY, USA. ²³Dana - Farber Cancer Institute, Boston, MA, USA. ²⁴These authors contributed equally: Tyler J. Aprati, Wei-Yu Chi. ²⁵Deceased: Stephanie H. Davis. ²⁶These authors jointly supervised this work: Alpaslan Tasdogan, David Liu, Ashley M. Laughney. ✉ e-mail: bi2175@cumc.columbia.edu



Extended Data Fig. 1 | See next page for caption.

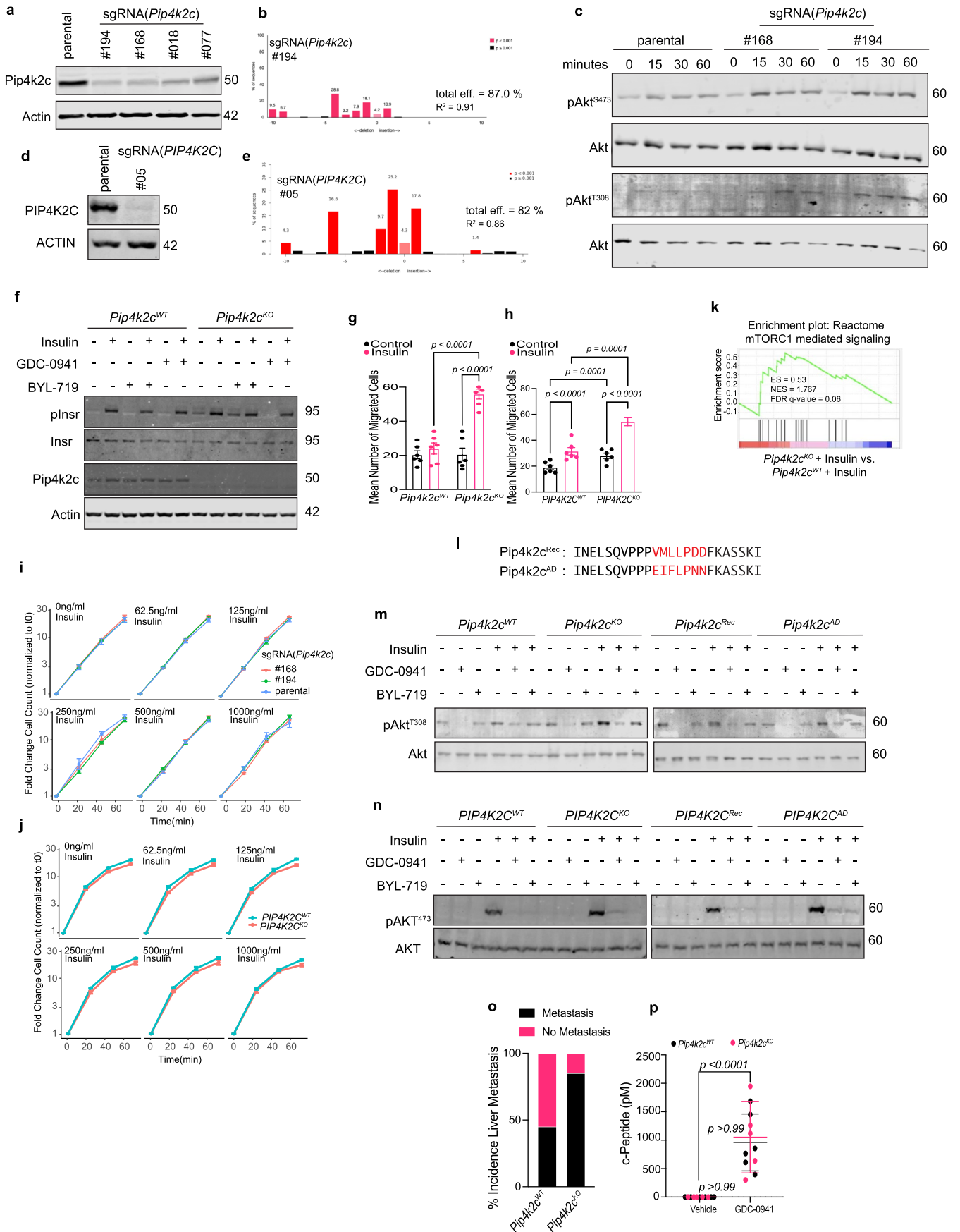
Extended Data Fig. 1 | Cas9 expressing HCmel12 melanoma cell line generation, mouse kinome (Brie) library titration and kinome (Brie) sgRNA representation at different steps of tumor cell editing, primary tumor growth, and metastasis. **a**, Assessment of Cas9-activity using an EGFP/EGFP-sgRNA-reporter using flow cytometry in HCmel12 melanoma with Cas9-expression, alongside HCmel12 melanoma cells expressing Cas9 without reporter (negative control), and parental HCmel12 cells without Cas9 but with reporter (positive control). EGFP-negative cells (rightmost plot) indicated activity of ~94%. **b**, Transduction of lentiviral library in Cas9-expressing HCmel12 melanoma cells. Percentage of tumor cells (y axis) transduced with the Brie library at virus dilutions (x axis). **c**, Proportion of cells calculated to be infected by one sgRNA-containing viral particle (y axis) at different dilutions of the Brie library (x axis). Filled graphs in (**b,c**) indicate viral concentration/dilution

used for the large-scale CRISPR screen. **d**, Pearson correlation coefficient of the normalized sgRNA read counts from Brie plasmid pool, transduced cells in vitro edited over time (10, 14, 21, 28, 35, 42, 49, 56 days after spin infection), from primary tumors (n = 8), from liver (n = 14), lung (n = 3), and lymph node (n = 8) metastases. For each biological sample type, biological replicates (R1, R2, R3... R8), for technical replicates (R3.1, R3.2) are shown. n = 8 mice for primary tumors, n = 7 mice with Liver mets, n = 3 mice with lung mets, n = 7 mice with LN mets. **e**, Boxplot of the normalized sgRNA read counts as in (d). Outliers are shown as colored dots for each respective sample. **f**, Principal-component analysis (PCA) of normalized sgRNA read counts. X- and y-axis with indicated explained variance of 49.7% and 5.4%, respectively. Samples from Brie plasmid, cells and primary tumors are shown in black while metastases are shown in red. Data is representative of two independent experiments.



Extended Data Fig. 2 | CRISPR/Cas9 viability screen in HcMel12 melanoma cells in vitro, Identification of essential genes and genes affecting engraftment of tumor cells in vivo followed by Identification of genes affecting liver tropism. a, b. LFC for all four individual sgRNAs targeting genes enriched (red lines) or depleted (blue lines) in cells vs plasmid (a), and primary tumor vs cells before transplantation (b), are depicted. The top and bottom 10 enriched or depleted genes are labelled with gene symbols. c. Tumor growth curves in mice transplanted with Cas9 (n = 5 mice) or Brie-transduced

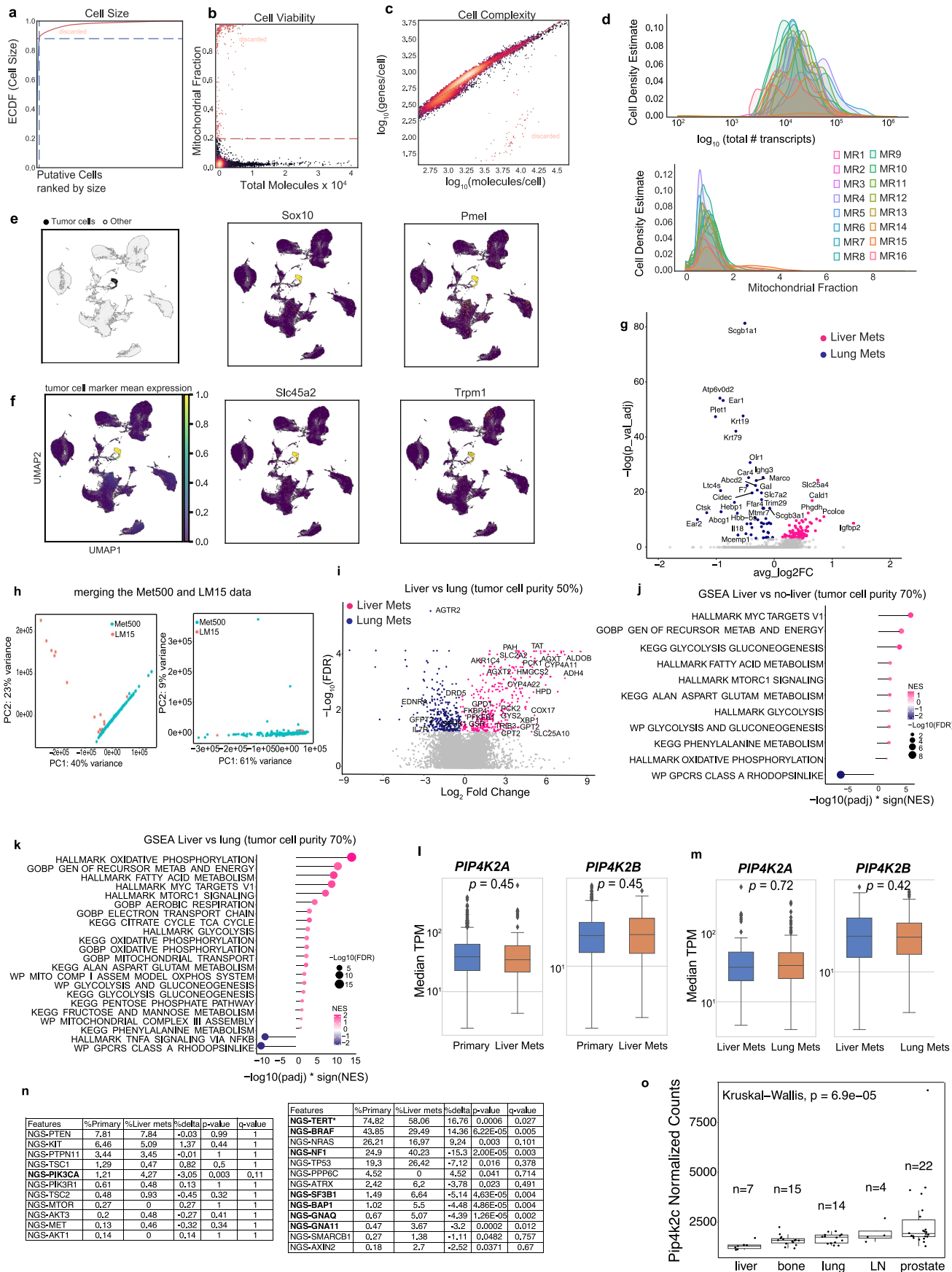
(Cas9 + Brie) HcMel12 melanomas (n = 10 mice) are shown; mean ± s.e.m. d. Bar graphs showing enrichment of sgRNAs targeted genes in among sgRNAs in liver metastasis. For each of the 14 individual liver metastasis samples (rows) harvested from 7 individual mice, the abundances of sgRNAs reads as a proportion of all reads are shown. Only target genes with at least 2% of the total reads in a sample are shown. e. Venn diagram showing the overlap of enriched sgRNAs in indicated comparisons with FDR < 0.06. Data is representative of two independent experiments.



Extended Data Fig. 3 | See next page for caption.

Extended Data Fig. 3 | Generation and validation of CRISPR knockout cells in vitro. **a**, Immunoblot showing efficacy of CRISPR-Cas9-mediated knockout of *Pip4k2c* using four sgRNAs. **b**, Resulting insertions/deletions for *Pip4k2c* sgRNA #194 analyzed by Sanger sequencing with Tracking of Indels by Decomposition (TIDE <https://tide.nki.nl>) and estimated efficiency of Cas9-mediated cuts. **c**, Immunoblots of phosphorylated and total AKT at two phosphorylation sites pAktS473 and pAktT308 in parental and two of *Pip4k2c* KO clones over time. **d,e**, Immunoblot showing efficacy of CRISPR-Cas9-mediated knockout of *PIP4K2C* using guide #5 in human A375 melanoma cell lines (**d**) and resulting indels (**e**) as in (**b**). **f**, Immunoblot of HcMel12 parental or *Pip4k2c* KO cells treated with insulin, and/or GDC-0941 (0.1 μ M) or BYL-719 (1 μ M). Blotted is the total abundance of insulin receptor (Insr) and phospho-Insr. **g**, Effect of insulin treatment on migration potential measured by transwell assay. Shown is the mean number of migrated parental and *Pip4k2c* KO cells with and without insulin treatment. $n = 3$ replicates per condition; mean \pm s.e.m. **h**, Same as in (**g**) for A375 melanoma cell lines. **i,j**, Proliferation assay of HcMel12 (**i**) or A375 (**j**) *Pip4k2c* WT and *Pip4k2c* KO melanoma cells at different insulin concentrations over time. Cell counts were normalized to t0 proliferation is shown as fold change.

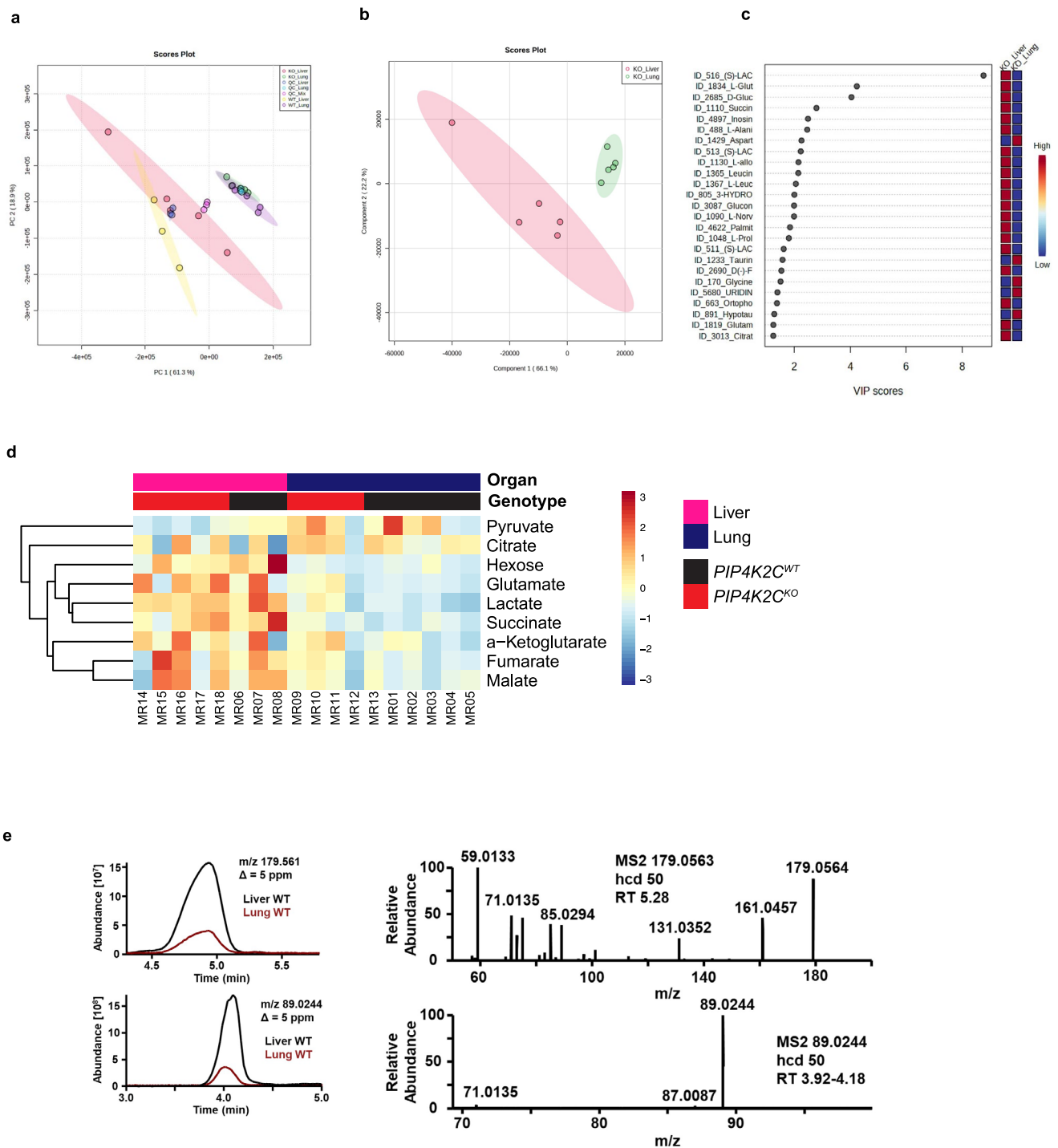
$n = 3$ replicates per condition; mean \pm s.e.m. **k**, Gene set enrichment analysis of RNA-seq data comparing *Pip4k2c* KO with parental cells stimulated with insulin. Exemplary pathway enrichment for mTORC1 is shown. **l**, Amino acid sequence of wild-type ORF (top) and allosteric domain-deficient (AD) *Pip4k2c*. **m,n**, Immunoblots showing phospho-AKT in parental, *Pip4k2c* KO, and *Pip4k2c* KO rescued with either wild-type *Pip4k2c* allele (*Pip4k2c* Rec) or allosteric domain-deficient (*Pip4k2c* AD) and combinatorial exposure to insulin (250 ng/ml, first row) and PI3K inhibitor GDC-0941 (0.1 μ M, second row) or BYL-719 (1 μ M, third row) in murine HcMel12 (**m**) or human A375 (**n**) melanoma models. Samples are derived from the same experiment and gels/blots were processed in parallel. **o**, Incidence of liver metastasis in mice bearing A375 *PIP4K2C* WT and *PIP4K2C* KO melanoma cells, $n = 10$ mice per group; **p**, C-peptide levels (in pM) for *Pip4k2c* WT and *Pip4k2c* KO HcMel12 tumor-bearing animals with and without GDC-0941 treatment. Plasma was collected after 2 hours of treatment with GDC-0941 and vehicle treatment was used as control, $n = 5$ mice per group. Statistical significance was determined using 2-way ANOVA Tukey's multiple comparisons test for (**g,h,p**). Data is representative of two independent experiments (**g,h,i,j,o,p**). Significance levels as indicated.



Extended Data Fig. 4 | See next page for caption.

Extended Data Fig. 4 | Validation of findings in mouse and human metastatic samples using scRNA-seq and Bulk RNA-seq. a-c. Quality control plots for single cell RNA sequence data. Cells were filtered based on (a) cumulative number of transcript counts, (b) fraction of mitochondrial mRNA detected per cell and (c) cell complexity as described in the Methods; shown here for one representative library. **d.** Kernel Density Estimate (KDE) plots showing distribution across cells of total number of transcripts (top) and mitochondrial fraction (bottom) for each sample. **e,f.** UMAP projections showing the tumor cell population, mean log-transformed gene expression of tumor cell marker gene signature, and log-transformed expression of select individual tumor cell marker genes. **g.** Top differentially expressed genes in liver metastasis (pink) vs lung metastasis (purple) tumor cells. Genes are projected by the $-\log_{10}(p_{adj})$ by the $averagelog_2(FC)$ and the most significant DEGs are labelled ($p_{adj} < 0.05$, Wilcoxon test). **h.** PCA of LM biopsy data across cancer types from Met500 and additional LM from melanoma patient biopsies (LM15) generated in this study pre- or post-batch correction with ComBat_seq (Methods). **i.** Differentially expressed genes in liver ($n = 78$, Met500; $n = 15$, LM15, pink) vs lung ($n = 16$, Met500, purple) metastases from patients across cancer types. Genes are projected by average \log_2 Fold Change by the $-\log_{10}(FDR)$ with genes significantly enriched ($FDR\ q\text{-value} < 0.05$, Mann-Whitney test) in liver (pink) and in lung (purple) metastasis tumor samples, with specific genes of

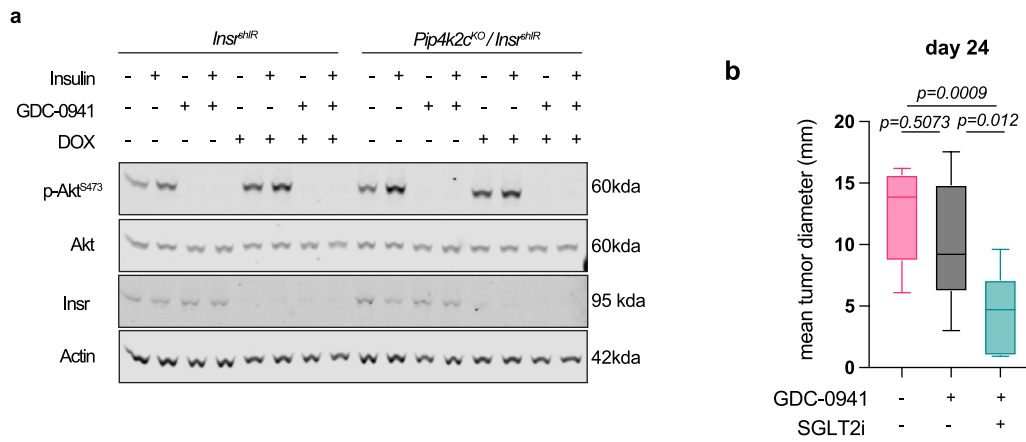
interest labelled. **j.** Pathway enrichment analysis ($FDR\ q\text{-value} < 0.05$, GSEA) in liver ($n = 41$, Met500; $n = 15$, LM15, pink) vs non-liver ($n = 100$, Met500, purple) metastases including only with 70% tumor cell purity. **k.** Pathway enrichment analysis ($FDR\ q\text{-value} < 0.05$, GSEA) in liver ($n = 41$, Met500; $n = 15$, LM15, pink) vs lung ($n = 9$, Met500, purple) metastases including only with 70% tumor cell purity. **l,m.** Expression levels of *PIP4K2A/B* in primary tumors vs. liver metastases (**l**) and liver vs. lung metastases (**m**). **n.** Frequency of genomic alterations across primary cutaneous melanomas and liver metastases from Caris melanoma patient cohort. The left table summarizes the frequencies between primary tumors and liver metastases for selected genes in the PI3K/AKT pathway, along with adjusted p and q values (methods), and the right table indicates unbiased analyses across all interrogated gene mutations among the same sites. **o.** Expression of *Pip4k2c* in primary prostate cancers, lymph node, lung, bone and liver metastases from the Arriaga et al. cohort; for all box plots, n refers to the number of samples, and p refers to the p-value. The center line indicates the median, the box limits denote the first and third quartiles, and the whiskers indicate the lowest or highest data points at the first quartile minus or plus 1.5 times the interquartile range. Statistical significance was determined using Frequency of genomic alterations: Mann-Whitney U Two-tailed test for (**l**, **m**) and chi-square or Fisher's Exact for (**n**). Significance as indicated.



Extended Data Fig. 5 | Metastatic site influences tumor cell metabolic state.

a, Score plot of a PCA analysis of all putatively identified metabolites by LC-MS in positive ionization mode. **b**, Score plot of a PLS-DA analysis of putatively identified metabolites by LC-MS in negative ionization mode comparing liver and lung metastatic samples from animals with A375 human melanomas with indicated genotypes (Methods). **c**, VIP score plot generated based on a PLS-DA of putatively identified metabolites by LC-MS in negative ionization mode comparing liver and lung metastatic samples from animals with A375 human melanomas with indicated genotypes, showing a strong change in lactic acid, glutamic acid and a hexose (for example glucose) that is causing the separation of the groups in **(b)**. **d**, Heat map of results from a suspected targeted analysis. Compounds were manually identified in the LC-MS data based on MS1 accurate mass and MS2-spectrum. The corresponding peaks were integrated, and the

results normalized by 13 C2-Citric acid that was spiked to the sample as an internal standard. The compounds were selected based on the multivariate data analysis indicating a change in the glycolysis and/or TCA cycle, disease site, liver ($n = 8$ specimens) vs. lung ($n = 10$ specimens); and genotype, parental [*PIP4K2C* WT] and [*PIP4K2C* KO]. Statistical significance was determined using Two-tailed t-test for (d), Lactate ($p = 2.36727E-05$), Pyruvate ($p = 0.03$), Citrate ($p = 0.25$), α -Ketoglutarate ($p = 0.18$), Succinate ($p = 0.004$), Fumarate ($p = 0.04$), Malate ($p = 0.04$), Hexose ($p = 6.72275E-06$). **e**, Extracted ion chromatograms (left) and corresponding MS2 spectra of the putatively identified hexose (for example glucose) with an accurate mass for the [M-H]⁻ ion of 179.5610 (top) and of lactic acid with an accurate mass for the [M-H]⁻ ion of 89.0244 (bottom). Much lower intensities were detected in the lung samples compared to the liver samples (Right).



Extended Data Fig. 6 | Role of Pip4k2c loss in primary tumor growth and response to systemic therapies. a. Immunoblots in matched cell lines with indicated genotypes (top) and combinatorial exposure to insulin (250 ng/ml, first row), PI3K inhibitors GDC-0941 (0.1 μ M, second row), and Doxycycline (1 μ g/ml, third row). **b.** Combined tumor diameter at day 24 in treatment groups

across genotypes; n = 10 mice per condition. Box plots denote the minima, maxima and median. Experiment was repeated twice with similar results. Statistical significance was determined using One-way ANOVA Tukey's multiple comparisons test. Data is representative of two independent experiments (**b**). Significance levels as indicated.

Reporting Summary

Nature Portfolio wishes to improve the reproducibility of the work that we publish. This form provides structure for consistency and transparency in reporting. For further information on Nature Portfolio policies, see our [Editorial Policies](#) and the [Editorial Policy Checklist](#).

Statistics

For all statistical analyses, confirm that the following items are present in the figure legend, table legend, main text, or Methods section.

n/a Confirmed

- The exact sample size (n) for each experimental group/condition, given as a discrete number and unit of measurement
- A statement on whether measurements were taken from distinct samples or whether the same sample was measured repeatedly
- The statistical test(s) used AND whether they are one- or two-sided
Only common tests should be described solely by name; describe more complex techniques in the Methods section.
- A description of all covariates tested
- A description of any assumptions or corrections, such as tests of normality and adjustment for multiple comparisons
- A full description of the statistical parameters including central tendency (e.g. means) or other basic estimates (e.g. regression coefficient) AND variation (e.g. standard deviation) or associated estimates of uncertainty (e.g. confidence intervals)
- For null hypothesis testing, the test statistic (e.g. F , t , r) with confidence intervals, effect sizes, degrees of freedom and P value noted
Give P values as exact values whenever suitable.
- For Bayesian analysis, information on the choice of priors and Markov chain Monte Carlo settings
- For hierarchical and complex designs, identification of the appropriate level for tests and full reporting of outcomes
- Estimates of effect sizes (e.g. Cohen's d , Pearson's r), indicating how they were calculated

Our web collection on [statistics for biologists](#) contains articles on many of the points above.

Software and code

Policy information about [availability of computer code](#)

Data collection

For RNAseq data analysis the tximeta R package (version4.3) (Love et al. 2020) was used to import transcript-level quantification data quantified with Salmon package (Patro et al. 2017). CRISPR-Cas9 screens from the samples were analyzed using software packages MAGeCK and MAGeCKFlute. MAGeCK allows to analyze CRISPR/Cas9 screen data, and performs quality control, read count generation and normalization, calculated beta score to evaluate gene selection performance. MAGeCK's robust rank aggregation (RRA) method was used to identify significantly enriched or depleted CRISPR-screen hits in cells and tumors. MAGeCKFlute R package (Version 4.0.3) was used for data analysis and visualization. Cell Ranger (v6.0.2), scanpy (v1.7.2) was used For Single Cell Computational analyses. For GSEA was used ClusterProfiler (v3.16.1). For Bulk RNA sequencing data we used RTA (Illumina) for base calling and bcl2fastq2 (v 2.19) for converting BCL to fastq conversion, coupled with adaptor trimming. We performed a pseudoalignment to a kallisto index created from Human transcriptomes GRCh38 using kallisto (0.44.0). No custom algorithms were used in this study.

Data analysis

Prism 9 software was used for statistical analysis. Cellprofiler software was used for quantifying cell proliferation.

For manuscripts utilizing custom algorithms or software that are central to the research but not yet described in published literature, software must be made available to editors and reviewers. We strongly encourage code deposition in a community repository (e.g. GitHub). See the Nature Portfolio [guidelines for submitting code & software](#) for further information.

Data

Policy information about [availability of data](#)

All manuscripts must include a [data availability statement](#). This statement should provide the following information, where applicable:

- Accession codes, unique identifiers, or web links for publicly available datasets
- A description of any restrictions on data availability
- For clinical datasets or third party data, please ensure that the statement adheres to our [policy](#)

Source data information for main and extended figures is available. Gene expression data that support the findings of this study have been deposited in the Gene Expression Omnibus (GEO) under accession number GSE188391.

Previously published RNA sequencing data that were re-analyzed for the Arriaga cohort under accession number GSE143812 or for MET500 data can be found at this website: [https://xenabrowser.net/datapages/?cohort=MET500%20\(expression%20centric\)](https://xenabrowser.net/datapages/?cohort=MET500%20(expression%20centric)).

Metabolomics data have been deposited in the Metabolomics Workbench (the NIH Common Fund's National Metabolomics Data Repository (NMDR) website, the Metabolomics Workbench, <https://www.metabolomicsworkbench.org> where it has been assigned Study ID ST002851. The data can be accessed directly via its Project DOI: <http://dx.doi.org/10.21228/M8043D>) repository.

All other data supporting the findings of this study are available from the corresponding author upon reasonable request.

Research involving human participants, their data, or biological material

Policy information about studies with [human participants or human data](#). See also policy information about [sex, gender \(identity/presentation\), and sexual orientation](#) and [race, ethnicity and racism](#).

Reporting on sex and gender

Reporting on race, ethnicity, or other socially relevant groupings

Population characteristics jxiu@caris.com, submitting a brief proposal, and signing a data usage agreement."/>

Recruitment

Ethics oversight

Note that full information on the approval of the study protocol must also be provided in the manuscript.

Field-specific reporting

Please select the one below that is the best fit for your research. If you are not sure, read the appropriate sections before making your selection.

Life sciences Behavioural & social sciences Ecological, evolutionary & environmental sciences

For a reference copy of the document with all sections, see [nature.com/documents/nr-reporting-summary-flat.pdf](https://www.nature.com/documents/nr-reporting-summary-flat.pdf)

Life sciences study design

All studies must disclose on these points even when the disclosure is negative.

Sample size

Data exclusions

Replication

Randomization

Reporting for specific materials, systems and methods

We require information from authors about some types of materials, experimental systems and methods used in many studies. Here, indicate whether each material, system or method listed is relevant to your study. If you are not sure if a list item applies to your research, read the appropriate section before selecting a response.

Materials & experimental systems

n/a	Included in the study
<input type="checkbox"/>	<input checked="" type="checkbox"/> Antibodies
<input type="checkbox"/>	<input checked="" type="checkbox"/> Eukaryotic cell lines
<input checked="" type="checkbox"/>	<input type="checkbox"/> Palaeontology and archaeology
<input type="checkbox"/>	<input checked="" type="checkbox"/> Animals and other organisms
<input type="checkbox"/>	<input checked="" type="checkbox"/> Clinical data
<input checked="" type="checkbox"/>	<input type="checkbox"/> Dual use research of concern
<input checked="" type="checkbox"/>	<input type="checkbox"/> Plants

Methods

n/a	Included in the study
<input checked="" type="checkbox"/>	<input type="checkbox"/> ChIP-seq
<input type="checkbox"/>	<input checked="" type="checkbox"/> Flow cytometry
<input checked="" type="checkbox"/>	<input type="checkbox"/> MRI-based neuroimaging

Antibodies

Antibodies used

Pip4k2c Rabbit Polyclonal antibody (17077-1-AP, Proteintech), 1:1000
 Phospho Akt (Ser473) (D9E) XP Rabbit mAb (4060S), 1:1000
 Phospho Akt (Thr308) (D25E6) XP® Rabbit mAb (13038S), 1:1000
 Phospho p44/42 MAPK (Erk1/2) (Thr202/Tyr204) Antibody (9101S), 1:1000
 P44/42 Mapk (Erk1/2) (3A7) Mouse mAb (9107S), 1:1000
 Insulin Receptor β (4B8) Rabbit mAb (3025S), 1:1000
 Phospho-IGF-I Receptor β (Tyr1135/1136)/Insulin Receptor β (Tyr1150/1151) (19H7) Rabbit mAb (3024s), 1:1000
 β -Actin (E4D9Z) Mouse mAb (58169S), 1:2000

For secondary antibodies:

Goat Anti-Rabbit IgG Antibody, IRDye® 800CW Conjugated - 0.5 mg (926-32211, LI-COR Biosciences)
 Goat Anti-Mouse IgG Antibody, IRDye® 680RD Conjugated - 0.5 mg (926-68070, LI-COR Biosciences).

Validation

Western blot antibodies used in this study were extensively used in the literature for previous studies, validation blots are shown in the product information sheets on the Cell Signaling Websites.

Eukaryotic cell lines

Policy information about [cell lines and Sex and Gender in Research](#)

Cell line source(s)

A375, CT26 and HEK293T cells were purchased from ATCC.
 Hcme12 melanoma cells were kindly provided by Prof. Thomas Tuetting (Magdeburg, Germany).

Authentication

the cell lines were not authenticated

Mycoplasma contamination

Cell lines were routinely tested for mycoplasma contamination using Lonza MycoAlert Kit (Cat. # LT07-318).

Commonly misidentified lines (See [ICLAC](#) register)

None of the cell lines used in this paper were in the list of misidentified lines.

Animals and other research organisms

Policy information about [studies involving animals; ARRIVE guidelines](#) recommended for reporting animal research, and [Sex and Gender in Research](#)

Laboratory animals

All mice were purchased from Jackson Laboratory and/or Charles River.
 Six to eight-week-old wild-type female C57BL/6J (Charles River, Stock Number: 027), NOD/SCID/IL2gR (Jackson Labs, Stock Number: 005557) and/or BALB/c (Jackson Labs, Stock Number: 000651).
 Mice received a normal chow diet (PicoLab Rodent 20 5053 laboratory Diet St. Louis, MO) or a ketogenic diet (Thermo-Fisher AIN-76A) where indicated, with free access to drinking water.
 Animals were housed under the following conditions: 12-12 hour light-dark cycle, 21.1-22.2 C, 30-70% humidity.

Wild animals

No wild animals were used in this study.

Reporting on sex	All mice were female.
Field-collected samples	No field collected samples were used in this study.
Ethics oversight	All animal studies were performed under following IACUC approved animal protocols at Columbia University (AC-AABE6570) and Harvard Medical School (AABQ9616). The maximum subcutaneous tumor size permitted by IACUC at Columbia University and at Harvard Medical School is 20mm. This maximum tumor size was never exceeded in the studies.

Note that full information on the approval of the study protocol must also be provided in the manuscript.

Clinical data

Policy information about [clinical studies](#)

All manuscripts should comply with the ICMJE [guidelines for publication of clinical research](#) and a completed [CONSORT checklist](#) must be included with all submissions.

Clinical trial registration	N/A
Study protocol	N/A
Data collection	N/A
Outcomes	N/A

Plants

Seed stocks	N/A
Novel plant genotypes	N/A
Authentication	N/A

Flow Cytometry

Plots

Confirm that:

- The axis labels state the marker and fluorochrome used (e.g. CD4-FITC).
- The axis scales are clearly visible. Include numbers along axes only for bottom left plot of group (a 'group' is an analysis of identical markers).
- All plots are contour plots with outliers or pseudocolor plots.
- A numerical value for number of cells or percentage (with statistics) is provided.

Methodology

Sample preparation	For assessing Cas9 cell cutting efficiency in HCmel12_Cas9 expressing cells, EGFP positive cells were measured using flow cytometry.
Instrument	Data were acquired with FACSCanto flow cytometer (BD Biosciences)
Software	Data were analyzed with FlowJo software (v10 for Mac).
Cell population abundance	Experiments used pure cancer cell line cultures.
Gating strategy	GFP untransduced cells were used to set a negative gate.

- Tick this box to confirm that a figure exemplifying the gating strategy is provided in the Supplementary Information.